
Electronic Thesis and Dissertation Repository

6-20-2024 12:00 PM

Computational Modelling of Branching Arteriolar Networks using Constrained Constructive Optimization

Yuki Bao, *Western University*

Supervisor: Goldman, Daniel, *The University of Western Ontario*

Co-Supervisor: Frisbee, Jefferson C., *The University of Western Ontario*

A thesis submitted in partial fulfillment of the requirements for the Master of Engineering Science degree in Biomedical Engineering

© Yuki Bao 2024

Follow this and additional works at: <https://ir.lib.uwo.ca/etd>



Part of the [Biomedical Engineering and Bioengineering Commons](#), [Circulatory and Respiratory Physiology Commons](#), and the [Investigative Techniques Commons](#)

Recommended Citation

Bao, Yuki, "Computational Modelling of Branching Arteriolar Networks using Constrained Constructive Optimization" (2024). *Electronic Thesis and Dissertation Repository*. 10193.
<https://ir.lib.uwo.ca/etd/10193>

This Dissertation/Thesis is brought to you for free and open access by Scholarship@Western. It has been accepted for inclusion in Electronic Thesis and Dissertation Repository by an authorized administrator of Scholarship@Western. For more information, please contact wlsadmin@uwo.ca.

Abstract

The microcirculation plays a critical role in tissue blood flow distribution and is thus a topic of importance for understanding organ pathophysiology. As an alternative to experimental investigations of microvasculature, this thesis introduces a computational algorithm based on constrained constructive optimization (CCO) which aims to generate visually and statistically realistic branching arteriolar network architecture in healthy skeletal muscle tissue. The algorithm includes a list of user-specified adjustable model parameters to generate networks characteristic of different skeletal muscle tissues. Geometric (including mean vessel diameters, lengths, and numbers of bifurcations per order, Horton's Law ratios, and fractal dimension) and hemodynamic (Murray's Law exponent and hematocrit) properties of the generated networks matched experimental values from literature when compared for validation. The resulting algorithm is a valuable tool for investigating network architecture and blood flow in various skeletal muscles.

Keywords

Microcirculation, arterioles, arteriolar network, hemodynamics, geometry, topology, biosimulation, computational modeling, perfusion distribution

Summary for Lay Audience

Microvasculature refers to the smallest vessels of the cardiovascular system which embed and distribute blood flow to tissues. As the direct point of contact between the cardiovascular system and tissues, the microvasculature is a topic of focus in research on tissue pathophysiology. Experimental investigations into microvascular networks are often labor-intensive, due to the large number and varying sizes of microvascular vessels, and difficult to collect due to limitations in modern-day technology. Additionally, individual and tissue-specific differences in microvasculature make experimental findings difficult to generalize. Therefore, computational modeling of vessel networks has been explored as an alternative in microvascular research which may circumvent experimental limitations. In this thesis, we present a computational algorithm which was produced with two main goals: 1) the algorithm generates networks comparable to real life physiology, and 2) the algorithm may be adjusted to generate networks applicable to different tissues and experimental conditions. To achieve the first goal, the algorithm was written based on constrained constructive optimization (CCO), a popular algorithm for computationally generating visually and statistically realistic vessel network architecture. To achieve the second goal, the algorithm was made to rely on user-adjustable geometric and hemodynamic parameters which will alter the generated networks. In order to validate that algorithm accomplishes these two goals, first, networks were generated with user-adjustable parameters set to fit properties from different experimental datasets of healthy skeletal muscle arteriolar networks. Then, vessels within networks were labelled using the Strahler's and centrifugal ordering schemes, two common methods for grouping vessels of similar geometric/topological properties. Using these two ordering schemes, geometric and hemodynamic properties of vessels may be calculated over multiple levels within the generated networks. To evaluate how statistically realistic and adaptable the generated networks are, their geometric and hemodynamic properties were matched and compared, based on their user-adjustable parameters, to different experimental datasets of healthy skeletal muscle arteriolar networks. Results demonstrated that geometric and hemodynamic properties of the generated networks were similar to experimental values from different healthy skeletal muscle arteriolar network datasets. Notably, though it is commonly conceived in literature that both the Strahler's and centrifugal ordering schemes group vessels of similar properties, and are hence interchangeable, these ordering schemes provided different vessel groupings when applied to identical networks. In conclusion, the resulting CCO-based algorithm has been proven to generate realistic and adaptable networks based on application to various experimental skeletal muscle datasets, making it a valuable tool for investigations into skeletal muscle microvascular architecture and blood flow. It may also act as a good reference for future work in developing adaptable algorithms that can generate realistic networks for different vascular territories.

Co-Authorship Statement

Chapter 2 has been submitted and accepted for publication in the Journal of Applied Physiology. The algorithm for generating network architecture was coded by Yuki Bao, with modifications from Dr. Daniel Goldman. Dr. Daniel Goldman provided code for simulating blood flow within the generated network architecture, with modifications from Yuki Bao. Validation of the computationally generated networks was performed by Yuki Bao using experimental data compiled from literature, and heavily includes rat gluteus maximus microvascular data collected by Dr. Mohammed Al Tarhuni under the guidance of Dr. Dwayne N. Jackson and Dr. Daniel Goldman at Western University. Dr. Daniel Goldman, Dr. Jefferson C. Frisbee and Dr. Gonca Erdemci-Tandogan assisted in the interpretation of results and provided Yuki Bao with guidance for the project.

Acknowledgments

The years 2023-2024 contain unforgettable memories which have not only significantly influenced my academic career but also my development as a person. This thesis is the culmination of those past moments and contains work which would not have been possible without the kindness and support of the following people:

First and foremost, I'd like to thank my supervisors Dr. Daniel Goldman and Dr. Jefferson C. Frisbee for their continuous guidance throughout my undergraduate and graduate studies. They have devoted a lot of care towards my growth as a student and professional, and their wisdom has led me through many turbulent times. I'm grateful to have them as my supervisors. I'd also like to thank Dr. Gonca Erdemci-Tandogan for generously providing me with her time, resources, and expertise as a member of my advisory committee. Our meetings are always a pleasure and I've really enjoyed working with her.

I want to thank my fellow lab member Keith Afas for offering his patience and advice when I'm stuck in my work. He is a role model for what it means to be hard-working and makes working in the office a fun and productive experience. Additionally, I'd like to thank members of Dr. Lauren Flynn's lab who oftentimes drop by and say hi – they have cemented trivia on Tuesdays as a core experience in my calendar and have made my graduate school days brighter.

Finally, I would like to thank my sister Angelica Bao for her companionship these past two years. The late nights we've spent studying together and sharing worries gave me a lot of strength in moments when I felt lost. And I must thank my parents and extended family for supporting me throughout this academic journey and for reminding me where my roots lie.

While there are others I haven't mentioned in name – friends from childhood, close ones who are now far away, peers I've met through extracurriculars, the ladies who work at UWO food services, etc. – everyone's support has been invaluable to me, and I am endlessly grateful.

Table of Contents

Abstract.....	ii
Summary for Lay Audience.....	iii
Co-Authorship Statement.....	iv
Acknowledgments.....	v
Table of Contents.....	vi
List of Tables.....	viii
List of Figures.....	ix
List of Abbreviations.....	xi
Chapter 1.....	1
1 Introduction and Literature Review.....	1
1.1 The Cardiovascular System and the Microcirculation.....	2
1.2 Microvascular Network Properties.....	4
1.2.1 Vessel Types.....	4
1.2.2 Network Geometry and Topology.....	8
1.2.3 Network Hemodynamics.....	12
1.3 Modelling of Microvascular Networks.....	20
1.3.1 Experimental Measurement of Microvascular Networks.....	20
1.3.2 Computational Models Built from Anatomical Data.....	22
1.4 Thesis Aim and Contents.....	31
1.5 References.....	34
Chapter 2.....	41
2 Arteriolar Network Generation Based on Constrained Constructive Optimization Error! Bookmark not defined.	
2.1 Introduction.....	41

2.2 Methods.....	45
2.3 Results.....	62
2.4 Discussion.....	83
2.5 Summary.....	94
2.6 References.....	95
Chapter 3.....	99
3 Conclusion.....	99
3.1 Thesis Contributions.....	99
3.2 Future Directions.....	100
3.3 References.....	103
Appendix – Figure Permissions.....	104
Curriculum Vitae.....	111

List of Tables

Table 1: Summary of Model Parameter Variables and their definitions.	48
Table 2: The diameter (R_D), length (R_L), and bifurcation (R_B) ratios for centrifugal (left) and Strahler's (right) order, calculated using three different methods.	75
Table 3: Horton's Law ratios collected from literature for various types of tissues: skeletal muscle, non-skeletal muscle, and non-vascular tissue.	76
Table 4: Fractal dimension, calculated over varying levels of boxes using the box counting method, in which three individual networks are calculated and then averaged.	80

List of Figures

Figure 1	5
Figure 2	11
Figure 3	24
Figure 4	50
Figure 5	53
Figure 6	55
Figure 7	63
Figure 8	64
Figure 9	65
Figure 10	66
Figure 11	67
Figure 12	68
Figure 13	69
Figure 14	70
Figure 15	72
Figure 16	72
Figure 17	74
Figure 18	78
Figure 19	81

Figure 20	82
Figure 21	83

List of Abbreviations

CCO	Constrained constructive optimization
Nbif	The number of bifurcations within a generated network
Qperf	Total flow within each terminal arteriole
Aperf	Total tissue area perfused per terminal arteriole
γ	The Murray's law exponent, from the power law relationship between diameter and blood flow
expVal	A percentage value, where any daughter vessel with a diameter less than this percentage of the parent vessel's diameter is ignored.

Chapter 1

1 Introduction and Literature Review

In this thesis, we review the utility of computational microvascular network models as an alternative to, or an assistive tool for, experimental investigations in the microcirculation. Additionally, we explore how computational microvascular network models may be developed to simulate real life physiology more closely. For this purpose, we introduce an algorithm which attempts to generate visually and statistically realistic microvascular network architectures in different vascular territories and physiological conditions. After comparison of geometric and hemodynamic properties between microvascular networks from the algorithm and experimental literature data, it is concluded that the algorithm presented in this thesis performs well in generating microvascular architecture for various skeletal muscle tissues and may be used as a reference for future biosimulation work.

To provide a fulsome understanding of the underlying background and motivations of this thesis, chapter 1 will cover the following subjects: the microcirculation is introduced as an essential component of the cardiovascular system due to its importance in blood flow distribution at the tissue level; different vessel types composing the microcirculation are described, as well as various geometric structures the vessels may create (e.g., branching vs. arcading networks); finally, experimental and computational methods for acquiring vessel network models are reviewed, including a brief commentary on their strengths and weaknesses.

1.1 The Cardiovascular System and the Microcirculation

The cardiovascular system is composed of two main elements: the heart and blood vessels. With these two elements, the cardiovascular system facilitates the delivery of blood (a medium for oxygen/nutrients supply and waste removal) to all bodily tissues to ensure their proper functioning. The cardiovascular system's blood delivery pathway may be described as such: the heart pumps bulk flow through large vessels (arteries) towards a branching network of progressively smaller vessels (arterioles) which distribute blood into capillaries, a network of tiny vessels capable of facilitating exchange of nutrients/waste with tissues via diffusion. From the capillaries, the blood is collected by a mirroring branching network of progressively larger vessels (venules and veins), which return blood to the heart. This looping path is referred to as systemic circulation, as it is the route in which blood is pumped to provide nutrients and oxygen for all tissues throughout the body. The cardiovascular system also contains a second loop known as pulmonary circulation, in which the heart directs blood towards the lungs for re-oxygenation and removal of CO₂.

The cardiovascular system plays a critical role in homeostasis and is sensitive to all bodily changes, pathological or not. While the heart is known to pump at varying rates to match blood delivery to whole body demand (i.e., during exercise) (1), blood flow at the tissue level is primarily regulated by the microcirculation. The microcirculation refers to regions of the cardiovascular system composed of small vessels – i.e., arterioles, venules, and capillaries – which embed and thoroughly perfuse organs and functional tissue (2). While experimental identification of the microcirculation has varied between studies based on species, tissues, and physiological conditions, it is commonly defined by

a vessel diameter cutoff of approximately 100-300 μm (3–5). Due to its direct contact with tissue, the microcirculation is recognized as an essential region of study for understanding tissue and organ pathophysiology (6).

It has been hypothesized that during disease conditions, dysfunctional interplay between vasoregulatory mechanisms results in inefficient microcirculatory flow, which may exacerbate cellular dysfunction and disease progression within tissues and organs. In the microcirculation, arterioles are commonly recognized as the vessels which control the inflow and distribution of blood in tissues. Microcirculation studies have suggested that arteriolar regulation results from the integration of a vast array of stimuli – as examples, changing blood volume, hormones, electrolytes, osmolarity, chemical balances, etc. – which may originate from a range of sources such as the adrenal glands, kidneys, the parasympathetic and sympathetic nervous systems, or medications (7, 8). As a result of these stimuli, acute arteriolar regulation of blood flow may be accomplished via smooth muscle dilation or constriction of vessel diameter. Meanwhile, longer-term regulation may occur via vascular remodeling, resulting in changes in vessel composition or entire network structures. Attempts to study arteriolar behavior have resulted in the need for a large sample size of microvascular models, as arteriolar behavior has been observed to vary in different physiological states, such as disease or exercise, and appears to be tissue specific (9–11). Additionally, individual- and demographic- specific differences seem to exist due to highly diverse and variable cell expressions (12). Understanding the specificity of arteriolar behavior in various microvascular models is essential for resolving complex interactions between vasoregulatory mechanisms which induce the

observed behavior and discussing the relation between arteriolar regulation and tissue/organ pathophysiology.

1.2 Microvascular Network Properties

This section presents common properties of the microcirculation from past experimental work. Information within this section will aid in the consideration of what is a physiologically realistic network model, as most models used in microvascular research contain limitations towards simulating in vivo conditions as discussed in section 1.3.

1.2.1 Microvascular Vessel Types

The microcirculation constitutes a complex network of vessels with varying roles and properties. Though properties of vessels of the microcirculation are not fixed between species, tissues, and physiological condition, they may generally be classified into arterioles, venules, and capillaries based on shared characteristics, such as diameter, structural makeup, physiological role, etc. The approximate structural composition of arteriole, capillary, and venule vessel walls have been illustrated in Figure 1 and further described below.

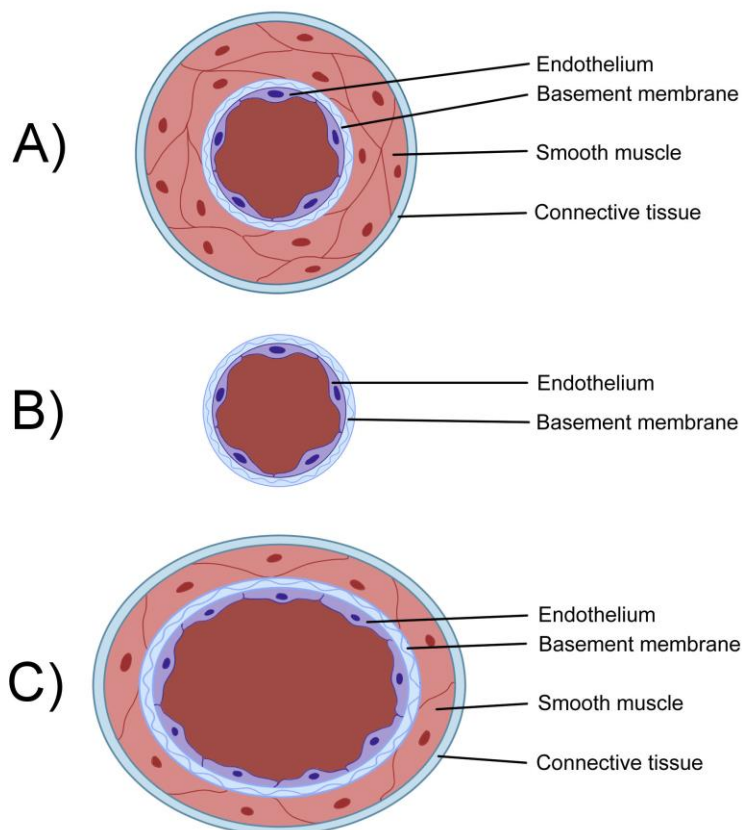


Figure 1. The approximate structural composition of A) arteriole, B) capillary, and C) venule walls. Differences may be observed in both structural composition and relative thickness of vessel walls.

Arterioles are commonly observed branching off from arteries and connecting to capillaries embedded in tissues, acting as the transition point between the macrocirculation and the microcirculation. In the cardiovascular system, they are the site of highest flow resistance and cause the greatest drop in blood pressure, hence their alternative name ‘resistance vessels’. Arterioles typically range in diameter from 10 to 200 μm . From inward out, arterioles consist of three main layers: the tunica intima

(endothelial cells sitting on a basement membrane), tunica media (smooth muscle), and tunica adventitia (thin sheath of connective tissue, which may contain collagen, nerve endings, and fibroblasts) (13). Typically, large arterioles will have two to four smooth muscle layers, the number decreasing as arteriolar diameter decreases. The structural makeup of arterioles may also vary slightly between tissues; for example, arterioles within expandable tissue such as skeletal muscle typically possess an additional external elastic lamina that allows arterioles to elongate or recoil with the tissue, which is missing in non-expandable tissue such as the brain (9). Arteriolar smooth muscles has been demonstrated to react in response to physical and chemical stimuli from various physiological sources (e.g., sympathetic innervation, parenchyma metabolism, endothelial cells, blood pressure, etc.) to constrict or dilate (7); as such, arterioles have been identified as the principal site of blood regulation to specific tissue areas and the gatekeepers of capillary beds, contributing to upstream perfusion pressure.

Capillaries are the smallest vessels of the cardiovascular system, ranging up to 10 μm in luminal diameter. In the microcirculation, capillaries are commonly found perfused by arterioles, drained by venules, and embedded within tissues/organs beside active cells and parenchyma; their proximity allows for exchange of nutrients to occur via diffusion, active cellular transport, and convection through the vessel wall according to tissue metabolic demand. From outside inward, capillaries consist of a single layer of endothelium surrounded by a basement membrane, lacking any smooth muscle. Their structural makeup is specialized to provide minimal diffusion distance between blood and tissue, enabling maximal exchange of certain molecules whilst blocking others. The number and geometry of capillaries also constitutes a large interfacing surface area to

facilitate this exchange (2). In the twentieth century, it was popularly theorized in August Krogh's capillary motor hypothesis that blood flow control resides principally in the capillaries, not arterioles (14); it was theorized that only a fraction of capillaries is perfused at rest, with more being recruited under periods of stress (e.g. hypoxia). The ability to recruit capillaries was attributed to the existence of precapillary sphincters which 'open' or 'close' the capillary lumen via constriction. However, the existence of precapillary sphincters has an absence of supportive morphological findings (15). Now, it is more commonly believed that tissue perfusion is the result of upstream arterial regulation. Though Krogh's capillary motor hypothesis has been largely disproven, capillaries may still contribute to blood flow control within tissues via structural adaptations (e.g. capillary pruning and angiogenesis) over long time scales, often in response to sustained physiological conditions such as hypoxia (16).

While an abundance of data is available on arterioles and capillaries, less research has been done on venules. Venules tend to be wider than arterioles but have thinner walls as blood pressure in venules is far lower. The composition of venule walls are similar to that of arterioles; but while larger venules may have a layer of smooth muscle within their media, smaller venules tend to be devoid of smooth muscle (2). Venule walls tend to be porous, so they also play a role in the exchange of oxygen and nutrients with tissues. The organization of venules is similar to arterioles, except venules tend to be wider and more numerous in comparison.

Though the microcirculation generally follows a pipeline of arterioles to capillaries to venules in a branching and reverse branching tree pattern, deviations are not uncommon. Oftentimes arterioles will directly connect to the venules, bypassing the

capillary bed. This may be observed within microcirculatory territories such as cutaneous perfusion and is known as the arteriovenous (A-V) shunt. A-V shunts play an important role in body temperature regulation due to their sympathetic innervation; sympathetic stimulation may induce constriction of arterioles, decreasing the volume of blood in the skin, to prevent heat loss (13). Other examples of growths which stray from the branching network pattern include anastomoses, multiple capillaries in series (rete mirabile), and arcades (12). For such growths, alternative classification schemes for vessel types within the microcirculation have been developed (17, 18).

1.2.2 Network Geometry and Topology

In the microcirculation, network structure has been recognized to be highly heterogeneous, with a great variety of shapes and sizes between different tissues and species (2, 12, 19). Tissue-specific differences exist to ensure that blood perfusion matches the functional requirements of the tissue. Meanwhile, individual-specific differences suggest that network growth is partially stochastic. Due to the irregularity of microvascular architecture, blood flow distribution within specific tissues cannot be fully understood without careful characterization of network geometry and topology. As such, this section will identify geometric/topological patterns which persist in the microcirculation despite its heterogeneity and review quantitative methods of characterizing network architecture.

A prominent topologic motif in vasculature is the branching pattern vessel networks form resembling tree branches or roots. This branching motif is commonly observed as arterioles transition into capillaries via diverging bifurcations and capillaries combine into venules as converging bifurcations. It is rare for vessels to branch into more

than two daughter vessels, with published cases only being seen in disease (20). This topological branching pattern may be considered a fractal property, due to its repeated appearance over multiple scale sizes, and has been taken advantage of in computational algorithms for modelling microvascular networks (Section 1.3.2). In order to characterize the geometry and topology of branching microvascular networks, a number of classification schemes have been introduced which group vessels of similar properties into 'orders'. Within literature, the two most commonly employed schemes are the 'centrifugal' and 'Strahler's' ordering schemes (10). Differences between the two ordering schemes have been described below and illustrated in Figure 2. Ordering schemes for non-branching networks, such as arcades, are not common within literature and are often study-specific (18), hence they have not been described.

The Strahler's (or 'centripetal') ordering scheme was first introduced by Arthur Newell Strahler in 1952 (21) as a modification of Robert E. Horton's work in classifying river networks (22). To begin, the Strahler's ordering scheme assigns order 1 to the terminal vessels of a network. Moving from the terminal vessels towards the feed vessel, if two daughters of the same order join, then the order of the parent is increased by one. If two daughters of different orders join, then the parent is assigned the higher of the two orders. Reminiscent of its origins, Strahler's order is purely dependent on the topology of networks. Hence, it is ideal for terminal arteriolar networks which are located near capillary beds. It is also ideal for asymmetric networks, as it is capable of appropriately assigning side branches with significantly smaller diameters to lower orders, while assigning neighboring branches with large diameters to higher orders. However, due to its purely topological nature, the Strahler's ordering scheme requires the identification of all

terminal vessels; if the vascular network is incomplete, as in the case of experimental studies or damaged tissue, then the Strahler's ordering scheme will struggle to group vessels with similar properties.

The centrifugal ordering scheme was developed by Mary P. Wiedeman in 1963 to be applied on the subcutaneous microcirculation of a bat's wing (23). Unlike Strahler's order, this ordering scheme assigns order 1 to the feed vessel of the network. Moving from the feed vessel towards the terminal vessels, the centrifugal order of either or both daughters will increase by one if one of the following conditions are satisfied: 1) if the bifurcation angle between them is sufficiently large, or 2) if the diameter of either or both daughters are sufficiently small compared to the parent. The centrifugal ordering scheme is capable of labelling vessels starting from different levels of the network, making it more effective at grouping similar vessels within incomplete networks compared to the Strahler's ordering scheme. However, the bifurcation angle and diameter criteria are subjective, with cut-off values varying between studies, and thus must be considered when comparing data from different studies and vascular territories.

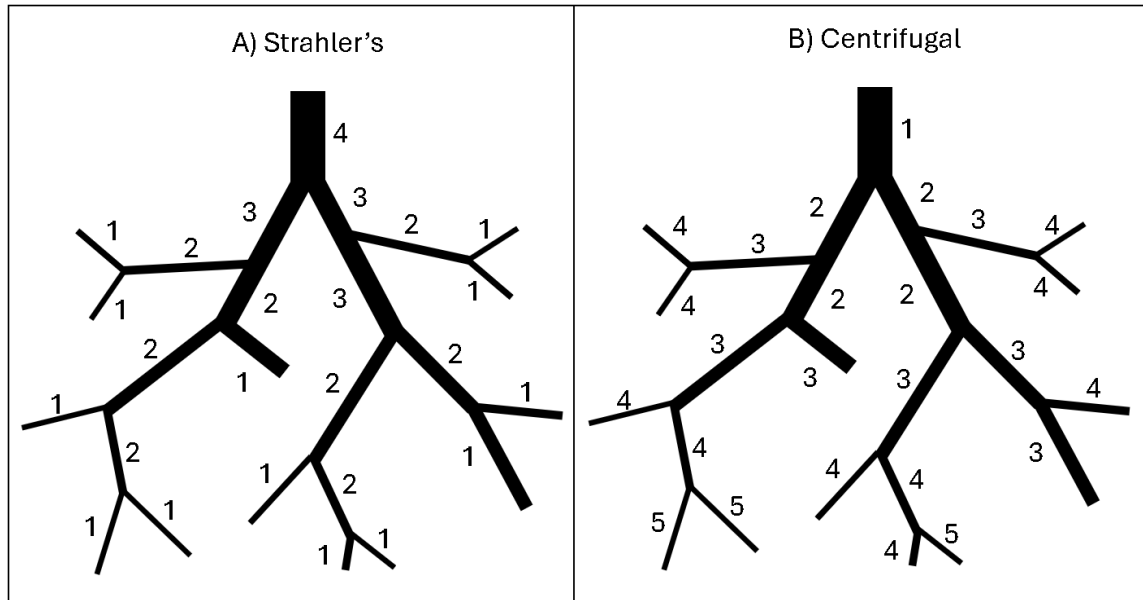


Figure 2. Comparison of centrifugal and Strahler's ordering schemes. In both panels, a simplified bifurcating network is labelled with centrifugal ordering in panel A, and Strahler's ordering in panel B. Differences between the two ordering schemes may be observed, especially at bifurcations with significant changes in daughter diameter/bifurcation angle.

As described, the Strahler's and centrifugal ordering schemes are not perfect solutions for classifying vessels in branching networks, each having their own strengths and weaknesses. Thus, modifications to both ordering schemes or new ordering schemes are commonly introduced across studies to better classify similar vessels into the same order (24, 25). However, common use of Strahler's and centrifugal ordering allows for comparison of data between studies and provides for a general understanding of vessel properties across generations in a network in spite of varying topologies. There is an additional benefit to using Strahler's ordering – experimental studies have demonstrated that there is a power law relationship that exists between Strahler's order and diameter,

length, and number of vessels within each order. This power law relationship is known as Horton's Law (26) and has been proven to hold true across various vascular territories (3, 17, 27, 28). Through Horton's Law, the slope of the linear fit between the logarithm transform of mean diameter, length, and number of vessels per Strahler's order has often been used to evaluate changes relative to the previous generation. These slope values are commonly known as the diameter, length, and bifurcation ratios, or cumulatively as Horton's ratios. The Horton's ratios may alternatively be defined as the ratio of mean diameter, length, or number of vessels from a higher order to an order one level lower. Methods for calculating the Horton's ratios when averaging over multiple networks have varied between studies, however value differences due to method are generally insignificant (3, 28).

Separate from ordering schemes, experimental studies have also demonstrated a power law relationship between blood flow and vessel diameter known as Murray's Law (29). The power law exponent has been demonstrated to typically range between 2 and 4, varying between vascular territories (30):

$$Q \propto D^\gamma \quad (1)$$

where Q is blood flow, D is vessel diameter, γ is the power law exponent. Murray's Law is particularly beneficial and commonly employed when considering the relationship between network geometry/topology and hemodynamics.

1.2.3 Network Hemodynamics

Flow within the cardiovascular system is primarily driven by pressure generated from the beating of the heart. The relationship between flow and pressure within any

closed system, whether it be a single vessel or the entire microcirculation, may be expressed using Ohm's law for fluid flow:

$$R = \frac{\Delta P}{Q} \quad (2)$$

where ΔP is pressure difference driving the flow, Q is the volume flow rate, and R is flow resistance. According to Ohm's law, flow resistance indicates the pressure required to sustain a given flow rate. Within a branching network of vessels, particularly within arterioles of the microcirculation, blood flow distribution and pressure drop depends on vessel resistances, which may be determined using rules analogous to circuits of electrical resistances: for elements in series (all carrying the same flow), e.g., an arteriole narrowing into a capillary without side branches, pressure drop is linearly proportional to the flow resistance of each element. Meanwhile, for elements in parallel (all subjected to the same pressure drop), as would be observed in a branching vessel network, the flow in each element is inversely proportional to their respective flow resistance. These rules allow for an understanding of blood flow distribution in vessel networks and demonstrate the influence of flow resistance on network hemodynamics. This is physiologically significant, as changing flow resistance via vessel diameter is the primary method of blood flow regulation employed by the cardiovascular system.

In the 1830s, Jean-Louis-Marie Poiseuille directly measured arterial and venous blood pressure to discover that pressure in venous vessels was lower than arterial vessels, irrespective of vessel size (12, 31). Thus, he concluded that pressure drop in the cardiovascular system must primarily occur within peripheral circulation. To further investigate the source of cardiovascular flow resistance, Poiseuille observed the flow of

simple fluids (i.e., distilled water) through long, narrow glass tubes using a range of controlled pressures (32–34). The main findings of his work eventually led to the derivation of an equation generally known as Poiseuille’s Law:

$$Q = \frac{\pi * r^4 * \Delta P}{8 * l * \eta} \quad (3)$$

Poiseuille’s law describes the relationship between dynamic fluid viscosity (η), pressure (ΔP) and flow (Q) within a cylindrical tube of length l and radius r . Poiseuille’s law holds true under several assumptions: the tube is uniform with a circular cross-section, and the fluid is Newtonian (with a fixed viscosity), steady (unchanging in time), and laminar (not turbulent). Though these assumptions rarely hold true in practice, Poiseuille’s law is still a useful approximation of blood flow in microvessels. Derivations of Poiseuille’s law has been published in other texts (33–35), however an informal understanding is as follows: by combining the Poiseuille flow assumptions with Navier-Stokes equations, which expresses conservation of mass and Newton’s second law for a fluid, the resulting fluid velocity profile becomes parabolic with radial position, being maximal at the tube center and zero at the wall. The coefficient of the parabola depends on pressure gradient ($\frac{\Delta P}{l}$) and fluid viscosity (η). The centerline velocity is proportional to the square of the radius (r). The volume flow rate (eq. 3) may thus be obtained by integrating velocity over the circular cross-sectional area.

When combining Ohm’s law (eq. 2) with eq. 3, Poiseuille’s law can alternatively be written as such:

$$R = \frac{8 * l * \eta}{\pi * r^4} \quad (4)$$

As observed from eq. 4, Poiseuille's law suggests that small changes in vessel radii result in large changes in resistance ($R \propto r^{-4}$); this is physiologically important, as it explains how arterioles are capable of regulating blood flow distribution within tissues via relatively small changes in vessel diameter.

While Poiseuille's law provides a fair approximation of flow in microcirculatory vessels and may be applied to the macrocirculation on average, individual macrocirculatory vessels do not display Poiseuille's law due to marked differences in hemodynamics. In large vessels, in the range of millimeters to centimeters, blood may be approximated as a homogenous Newtonian fluid – i.e., in addition to inertial effects, phenomena such as boundary layers, flow separation, instability, secondary flows, and turbulence may be observed (36). However, in the microcirculation, blood cannot be considered as a homogenous fluid since vessel diameters are not much greater than the cells it carries. Thus, flow dynamics in the microcirculation commonly considers blood as a multi-component fluid of primarily plasma and red blood cells (5, 12, 36). Another difference would be that the Reynold's number of the microcirculation is generally much smaller than 1, thus unlike in the macrocirculation. Thus, inertial effects are negligible and only laminar flow is observed.

The viscosity term from eq. 3, alternatively known as apparent or effective viscosity, applies to Newtonian fluids (fixed viscosity). However, as mentioned, blood cannot be considered as a continuum within microcirculation; the effects of red blood cell

deformation and aggregation within microcirculation causes blood to possess significant non-Newtonian properties. As such, experimentally measured values of blood viscosity often do not align with its apparent viscosity. A few important phenomena related to the noncontinuum nature of blood in the microcirculation are reviewed below. These phenomena are essential to understanding hemodynamics within microvascular networks and relevant to work described in Chapter 2 of the thesis.

The Fahraeus effect: As a result of behaving as a particulate, noncontinuum fluid in microvessels, a cell-free layer of fluid (predominantly plasma) may be observed near vessel walls when blood flows through. This phenomenon is referred to as the Fahraeus effect, named after Robin Fahraeus, who observed the effect in glass tubes in the early twentieth century (37). The cause for red blood cell aggregation at the centerline, away from the vessel wall, is not completely understood. However, a few hypotheses have been considered (12): first, the center of mass of each cell cannot approach the vessel wall closer than a certain distance; assuming red blood cells are approximately 2 μm thick, this approximates a cell-free layer of 1 μm . However, since the cell-free layer has been observed to be thicker, the migration of red blood cells has alternatively been explained via the mechanical interaction between the deformation of red blood cells and the surrounding nonlinear flow environment (38).

When observing the Fahraeus effect in microvessels, red blood cells migrate towards the centerline and flow at a faster velocity than the slow-moving cell-free layer near the vessel wall. As a consequence, the transit time of red blood cells is lower than would be expected in macrovascular flow. The Fahraeus effect is commonly mathematically described in terms of hematocrit, which is the volume ratio of red blood

cells to blood; the terms discharge hematocrit (H_D) refers to the hematocrit of blood within some reserve (i.e., macrocirculation), while tube hematocrit (H_T) refers to the hematocrit of blood flowing within a tube connected to the reserve (i.e., microcirculation). As such, the Fahraeus effect may be represented mathematically as follows:

$$H_D = \frac{Q_c}{Q_b} = \frac{H_T * v_c * A}{v_b * A} \quad (5)$$

Or alternatively:

$$\frac{H_T}{H_D} = \frac{v_b}{v_c} \quad (6)$$

where A is the cross-sectional area, Q_c and Q_b is the flow rate of red blood cells and blood respectively, v_c and v_b is the velocity of red blood cells and blood respectively.

While also known under the term ‘Fahraeus effect’, when vessel diameter is sufficiently small, typically around 10 μm , $\frac{H_T}{H_D}$ may suddenly increase – this phenomenon is specifically referred to as the ‘reverse Fahraeus effect’. It is hypothesized that this reverse effect occurs when vessel diameter is small enough to force red blood cells into single-file flow. Due to the physical limitations of red blood cell deformation, further decreases in vessel diameter results in narrowing of the cell-free layer, resulting in an increase to tube hematocrit (2).

The Fahraeus-Lindqvist effect: In addition to altering observed hematocrit values, the aggregation of red blood cells towards the centerline of microvessels also impacts blood viscosity. Due to the presence of the cell-free layer, blood viscosity in microvessels is

lower than as would be expected when compared to apparent viscosity (2, 36). Relative apparent viscosity is defined as the ratio of apparent viscosity to the suspending medium's viscosity – in the case of blood, the viscosity of plasma. In order to quantify blood viscosity in microvessels, Pries et al. (39) conducted a meta-analysis of numerous glass tubes experiments to yield a description of relative apparent viscosity (η_{vitro}) for suspensions of human red blood cells as a function of tube diameter and discharge hematocrit:

$$\eta_{vitro} = 1 + (\eta_{0.45} - 1) * \frac{(1 - H_D)^C - 1}{v_b} \quad (7)$$

where $\eta_{0.45}$ is the relative apparent blood viscosity for a fixed discharge hematocrit of 0.45, and C is the shape of the viscosity dependence on hematocrit:

$$\eta_{0.45} = 220 * e^{-1.3D} + 3.2 - 2.44 * e^{-0.06D^{0.645}} \quad (8)$$

$$C = (0.8 + e^{-0.075D}) * \left(-1 + \frac{1}{1 + 10^{-11} * D^{12}} \right) + \frac{1}{1 + 10^{-11} * D^{12}} \quad (9)$$

and D is the luminal vessel diameter.

Similar to the Fahraeus effect, a ‘reverse Fahraeus-Lindqvist effect’ may also be observed when vessel diameter is sufficiently low, where further decreases in vessel diameter is associated with an increase in viscosity (39).

Phase Separation at Bifurcations: When blood flows through a diverging branch point within microvascular networks, red blood cells and plasma may distribute non-proportionally between the daughter vessels, depending on each daughter's diameter. As a result, the discharge hematocrit of daughter vessels with the same parent may differ.

This effect is known as phase separation (5, 40). Over generations, phase separation leads to a large variation in hematocrit within a vessel network. Phase-separation also contributes to the ‘network Fahraeus effect’, which refers to the reduction of average discharge hematocrit in subsequent generations of a vascular network compared to the discharge hematocrit of the feeding vessel (12). The phase-separation effect was studied within the rat mesentery by Pries et al. (40) to yield the following empirical relation of blood and cell flow distribution at bifurcations:

$$\mathit{logit} FQ_E = A + B * \mathit{logit} \left(\frac{FQ_B - X_0}{1 - 2 * X_0} \right) \quad (10)$$

where the logit function may be defined as $\mathit{logit} x = \ln \left[\frac{x}{1-x} \right]$. The variables FQ_B and FQ_E refers to the fraction of parent blood and red blood cell flow that enters a daughter branch, X_0 is the critical blood flow fraction required to draw red blood cells into the daughter branch, B and A describes the nonlinearity of and difference between the red cell to blood volume flow relation. The variables A , B , and X_0 of eq. 10 may be further defined below (40):

$$A = -9.96 * \ln \left(\frac{D_\alpha}{D_\beta} \right) / D_f \quad (11)$$

$$B = 1 + 6.98 * \left(\frac{1 - H_D}{D_f} \right) \quad (12)$$

$$X_0 = \frac{0.4}{D_f} \quad (13)$$

Where D_α and D_β are the diameters of the daughter branches, D_f is the diameter of the parent vessel, and H_D is discharge hematocrit within the parent vessel. The cause of

phase separation has been again tied to the presence of the cell-free layer; the daughter vessel with the smaller diameter appears to draw flow predominantly drawn from the cell-free layer, an event known as ‘plasma-skimming’. As a result, the daughter with the larger vessel diameter will have a larger discharge hematocrit than the other daughter and the parent. The ‘pathway effect’ refers to the tendency of red blood cells to travel on long flow pathways through microvascular networks due to phase separation. Additionally, as vessel diameter become smaller in the peripheral circulation, there is the possibility that red blood cells will have difficulty entering the daughters – this phenomenon is called ‘red cell screening’ and contributes to the phase separation effect.

1.3 Modelling of Microvascular Networks

To understand disease progression in relation to the microcirculation, it is important to acquire a model of the vasculature of interest such that disease may be related to changes in the vasculature’s geometric/topological and hemodynamic properties. The following section will describe common experimental and computational means of acquiring microvascular models in the literature.

1.3.1 Experimental Measurement of Microvascular Networks

A review of the literature demonstrates that vascular network models are commonly acquired from experimental studies with a range of preparations (e.g., in vivo, in situ, in vitro) and models (e.g., different species, tissues, health conditions). The breadth of these experimental studies has enabled a general understanding of common vascular network properties. Additionally, these experimental studies allow for

developments in vascular biosimulation and other computational analysis work which may yield insights not normally acquirable using experimental methods.

Methods for measuring vascular structure and blood perfusion have been reviewed in previous studies, evaluating their strengths and weaknesses (41–43). Noninvasive assessment of microvascular function is limited based on accessibility of the microvascular network, and thus, is commonly performed in regions such as the skin, bulbar conjunctiva, sublingual mucosa, and retina. Intravital video microscopy remains one of the most commonly cited methods, as it is able to yield high resolution real-time video recordings of microvascular networks, from which network geometry, topology, and hemodynamics can be evaluated (3, 44). Another commonly mentioned method is laser Doppler flowmetry, which is advantageous in being noninvasive, cheap, and easy to use; however, its indirect measurement of blood flow requires complex analyses in order to interpret its results in a physiological context (45).

Experimental microvascular studies, while undoubtedly essential, are often accompanied by various difficulties. Some limitations may be inherent in the experimental procedure; for example, in situ setups may experience confounding factors from neighboring unobserved vascular networks. Additionally, modern day imaging methods, such as intravital video microscopy, are often limited in range of resolution based on the set magnification, which may lead to missing smaller or noisier vessel growths; this causes the collected data to represent an incomplete vascular network which may bias further analyses. It may be observed that most published data acquired from experimental microvascular studies features a limited vessel diameter range (10–40 μm) which may not be representative of the full vascular tree. Another point worth

considering is how collecting structural or hemodynamic data at multiple vessel levels in a vascular network, especially in smaller microvessels, remains labor-intensive. The fact that the applicability of collected microvascular data to other vascular territories (e.g., different tissues, species, etc.) is usually rather constrained only propagates the need for more experimental work.

The heterogeneity of microvascular networks, relating to their topology, morphology, hemodynamics, and functional parameters, has made it difficult to understand their properties and behavior on a vessel-to-vessel basis without a complete microvascular model. However, experimentally acquired microvascular models are difficult to attain and may contain limitations inherent in experimental procedures. Hence, computational models have been explored as an alternative or assistive tool in microcirculation studies. Computational models have been proposed to be capable of capturing missing data from experimental studies while being less labor-intensive to produce and replicate across various demographics of vascular tissues.

1.3.2 Computational Models Built from Anatomical Data

Computational models of microvascular networks are analogous to experimental models, in that they contain network architecture and hemodynamic information which may be used for hypothesis testing. Unlike experimental studies, modelers themselves must decide how to specify the network's geometric/hemodynamic properties such that they will be physiologically realistic. Methods for doing so as mentioned in literature will be reviewed in this section. This section will address two challenges when designing a

computational network model: 1) how to describe realistic microvascular network structures and 2) how to simulate blood flow within those structures.

1) Generating geometrically/topologically realistic network structures:

While various algorithms for generating the vascular network geometric/topological structure have been proposed, few have been able to replicate the considerable amount of irregularity and randomness that is evident in experimental observation of microvascular beds. Often, microvascular networks are approximated using simplified network topologies; a common and straightforward representation depicts them as a series of merging and unmerging vessels, with vessels of the same ‘category’ (e.g., arterioles, capillaries, venules) arranged in parallel (46, 47). Figure 3 depicts an example of such a network.

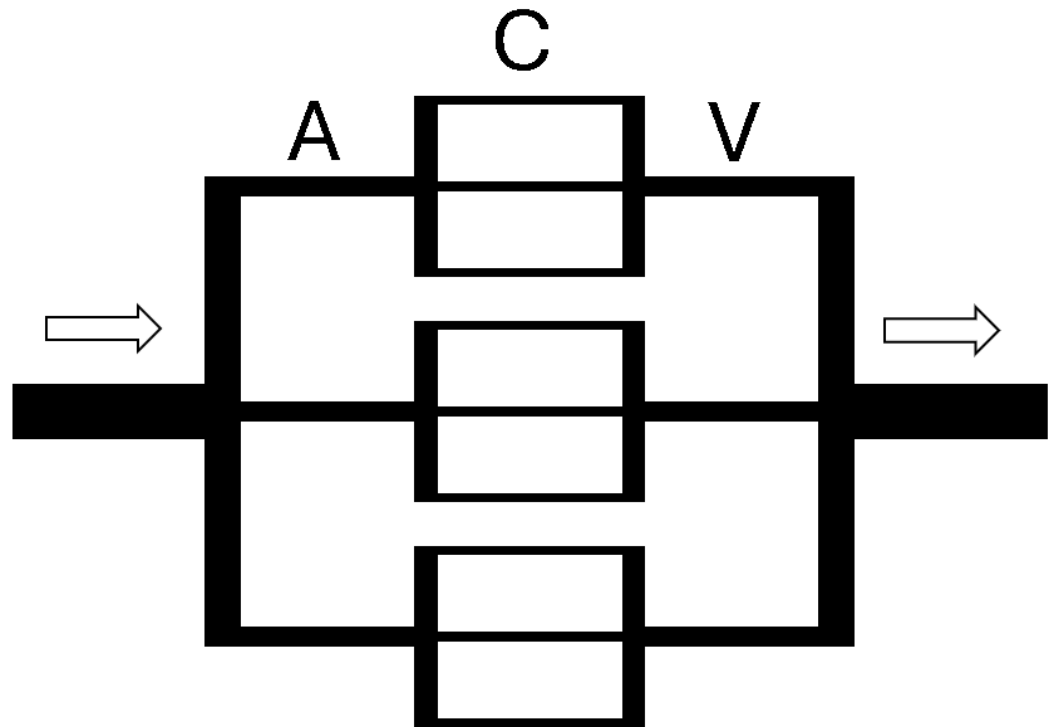


Figure 3. An idealized representation of a microvascular network. The microvascular network is represented as a series of vessels organized into different ‘categories’, where vessels of the same category are displayed in parallel. Arrows represent the direction of blood flow, while A represents arterioles, C represents capillaries, and V represents venules.

While these simplified topologies may be sufficient for a statistical approximation of certain network properties, the heterogeneity in real life vascular network architecture strongly impacts resulting hemodynamics, which may impact vascular function. For example, geometric heterogeneity (vessel length and diameter) within microvascular networks influences mean network hematocrit, while topological heterogeneity (vessel connections) has been strongly correlated with network conductance and pressure

distribution (4, 48). Additionally, spatial heterogeneity of microvascular flow distribution in tissues, which was linked to vessel diameter, is increased in physiological conditions such as metabolic syndrome (11). As such, computational models should aim to take the heterogeneity of microvascular geometry/topology into consideration when designing model architecture.

One proposal for producing realistic microvascular models would be to simply generate the models from experimentally acquired imaging data; within this thesis, these models henceforth will be referred to as ‘anatomical’ models. An example would be machine learning-based segmentation of images acquired via magnetic resonance angiography to identify and generate vasculature (49). However, while anatomical models provide an accurate representation of the coarse structure, they possess many of the same limitations as experimental models by depending on the availability of imaging data. Additionally, since anatomical models are generated to identically match image data, they struggle in being applied to other vascular territories; there is no adjustment parameter that will allow for adaptation of the generated vasculature to different species, tissues, and disease conditions.

Both experimental and anatomical models rely on the availability of experimental data and consequently struggle from limitations inherent in experimental procedures. Thus, a relatively new approach has been proposed in literature: to circumvent experimental limitations, and to create models which are adaptable to different vascular territories, computational models may be developed based on experimentally-derived mathematical relations rather than experimental data. Examples of such mathematical relations, which may describe microvascular geometric/topologic and hemodynamic

network properties, are included in sections 1.2.2 and 1.2.3. These mathematical relations allow for the generation of models which act in compliance with physiological criteria and morphometric constraints. The goal of computational models constructed thusly is for the generated networks to be statistically consistent with experimental data in reproducing geometric/topological features, functional responses, and heterogeneity of real vascular networks, without direct reliance on experimental data.

Within the literature, two classes of algorithms for the automatic generation of vascular beds are commonly explored: fractal and space-filling algorithms. Fractal algorithms have been used to produce self-similar models which have been reported to successfully follow many statistical properties of real vascular trees (e.g., vessel radius, length, aspect ratio, and bifurcation angle); however, real vascular networks grow too stochastically to produce such perfectly replicating patterns (50, 51). Meanwhile, space-filling algorithms allow for the generation of a vessel network within some pre-defined vascular territory in 2D or 3D space. While various interpretations of such algorithms have been proposed, the most popular approach to a branched arterial system is the constrained constructive optimization (CCO) algorithm, originally introduced by Shreiner (52, 53). CCO is based on the principle of optimum design, where the goal is to minimize some chosen cost function – e.g., blood volume or vessel path length (54). A CCO-based vascular tree is grown by successively adding new terminal segments while maintaining a set of physiological boundary conditions and constraints typically informed by experimental data; at each step of growth, geometric location of the new connecting segment and topology of the existing network is optimized according to a chosen cost function (e.g., blood volume of the vascular tree at the given step of growth). Through

CCO, the generation of realistic arterial model trees in full detail (including location, length, and diameter of vessel segments) can be performed across a large spatial scale. Validation of CCO-based algorithms with experimental data has demonstrated that CCO can reproduce the correct spatial arrangement of main arteries and the topology of the complete arterial system down to the capillaries (55, 56). Due to the detailed geometric information provided by CCO, blood flow simulations may also be performed in CCO-based models as reviewed in the latter half of this section.

CCO has been used to address various types of study, ranging from anatomical variation (56–59), network fractality (60, 61), shear stress distribution (62, 63), and others. An overview of current CCO usage in literature will be presented in the following paragraph: certain CCO variants have been proposed to recreate (61, 64–68) or speed up (66, 69) the generation of more complex vascular networks in hollow organs. Attempts to address more physiologically realistic scenarios have been made by using CCO to simulate territories supplied by multiple inlet vessels: partitioning of a territory into subdomains was proposed so CCO could independently be applied to vascularize non-overlapping subdomains (66, 70, 71), or alternatively, Jaquet et al. proposed that a flow quota could be assigned to each inlet vessel, where vessels that temporally exceed their quota are put on hold (66, 72). Certain research has attempted to create patient-specific vascular models by combining image data with CCO, where patient vasculatures are segmented from the images to create a base model, and CCO is used to extend the image-based model downwards to space-fill the uncaptured smallest vessels (67, 72). Latest works using CCO have focused on generating microvasculature for whole organs, defining multiple ad-hoc steps to generate vasculature accurate to different tissues in

organs (67, 73). Certain investigations have attempted to use CCO to address the need for a versatile vascular model that can be adjusted to suit vessel networks across various physiologies. For example, Talou et al. introduced an adaptation of the CCO algorithm termed adaptive constrained constructive optimization (DCCO) which integrates an adaptive optimization criteria and multi-staged space-filling strategies to produce models for various vascular territories of varying complexity (74).

2) Calculating blood flow within a given network structure:

Blood flow simulation methods must always cater to how microvascular network architecture is defined. If the network is traced from imaging data to include irregularities such as the vessel lumen, rather than idealized into simple shapes, math for calculating hemodynamic parameters can become very complex.

Computational microvascular network models often employ compartmental “branching tube” representations of blood vessels. In other words, microvascular vessels are idealized into straight cylindrical tubes within which blood flow calculations may be performed. In all aforementioned methods for generating microvascular network architecture (i.e., experimental, anatomical, and automatic generation), branching tube representations of blood vessels may be used. Pries et al. attempted to quantify the hemodynamic effects of diameter irregularity, demonstrating that the difference between predictions of vessel resistance from branching tube models and experimental measurements increases as vessel diameter decreases, from less than 5% at 20 μm to around 20% below 10 μm (75). Hence, though microvascular vessels are indeed not idealized cylindrical shapes, it remains a decent approximation for vessels above 10-20

μm . Additionally, the assumption is convenient, as it allows for the calculation of hemodynamic parameters within microvessels via previously derived (originating from glass tube studies and demonstrated in vivo) and commonly used equations describing microfluidic behaviors, such as the Fahraeus-Lindqvist effect, the Fahraeus effect, and phase separation (section 1.2.3).

Using the branching tube assumption, one of the most popular methods for simulating blood flow and hemodynamic parameters within an entire vascular network is described in Pries et al., 1990 (5). The method consists of two procedures, which are carried out alternately until the final blood flow solution is reached. The first procedure involves the calculation of blood flow in each vessel segment and pressure at each node (coordinates at the start and end of each segment). For the first run, some initial guess of unknown rheological parameters may be used; more accurate guesses will result in faster computation (less iterations) of the blood flow simulation solution. The first procedure starts by assuming conservation of flow at any node, i.e., that the sum of inflowing and outflowing blood at the center node of any bifurcation (or ‘bifurcating’ node) is zero:

$$\mathbf{Q}_1 + \mathbf{Q}_2 + \mathbf{Q}_3 = \mathbf{R}_1 * (\mathbf{P}_0 - \mathbf{P}_1) + \mathbf{R}_2 * (\mathbf{P}_0 - \mathbf{P}_2) + \mathbf{R}_3 * (\mathbf{P}_0 - \mathbf{P}_3) \quad (14)$$

where \mathbf{Q}_1 and \mathbf{R}_1 is the blood flow and resistance within the parent segment. \mathbf{P}_0 and \mathbf{P}_1 are the start and end nodes of the parent segment. \mathbf{Q}_2 and \mathbf{Q}_3 , \mathbf{R}_2 and \mathbf{R}_3 , and \mathbf{P}_2 and \mathbf{P}_3 are the blood flows, resistances, and pressure at the end nodes of the daughter segments. Eq. 14 may be used to construct a system of linear equations for every bifurcation in the network, solving for pressures at every node (assuming pressures at the start node of the feed vessel and the end node of each terminal vessel is known). This

system of linear equations may become lengthy with large networks, however it can easily be solved using equation solvers, which are available in most programming libraries, or the iterative method of successive overrelaxation (76).

The second procedure involves the computation of discharge hematocrit and apparent viscosity of each segment, using blood flow and pressure values from the first procedure. Conservation of blood flow and red blood cell flow rates is applied at every node to form a system of equations, assuming discharge hematocrit and apparent viscosity is known in the feed vessel. This system of equations may also be solved using successive overrelaxation. Phase separation effects (eq. 10-13) are integrated with the system of equations for the calculation of discharge hematocrit and viscosity; however, these equations require values from the parent vessel. Thus, the calculation of the second procedure must occur from upstream to downstream. This may be performed by assigning a label to each vessel in the order of decreasing pressure, which would correspond to how far from the feed vessel the vessel is and, running calculations in the order of the labels. Once discharge hematocrit has been calculated, relative apparent viscosity may be solved using the Fahraeus-Lindqvist effect (eq. 7-9). Tube hematocrit may be calculated from the Fahraeus effect (eq. 5). Finally, blood flow and hematocrit are adjusted based on the error between the current and previous iteration; these updated values will be fed into the first procedure in the subsequent iteration. By iterating the two procedures, where hemodynamic values are updated based on error between every loop, a solution is reached when there is convergence – i.e., the hemodynamic solution is no longer changing with each iteration within some level of tolerance.

While section 1.3.2 has focused primarily on branching tube representations of blood vessels and the blood flow simulation method described by Pries et al., 1990, many other theoretical models exist for simulating blood flow in individual vessels or entire networks; certain areas of interest within microcirculatory blood flow simulation include the impact of interactions between red blood cells, pressure wave propagations within blood, and blood flow in tortuous and irregular vessel geometries (77, 78). Additionally, while blood flow simulations often focus on red blood cells and plasma, the impact of other blood components (e.g., white blood cells) have also been explored (79, 80).

1.4 Thesis Aim and Contents

This thesis presents an approach addressing a major challenge relating to the computational simulation of real-life vasculature: the generation of vascular networks with realistic geometric/topological structure. The following chapter of this thesis will walk through the step-by-step development and validation of a CCO-based simulation code which generates geometrically/topologically realistic computational models of microvasculature within rat skeletal muscle tissue. The aim of this thesis is to provide a framework for future development of computational models which can generate realistic vasculature within different tissues, as such work will be conducive to yielding an alternative method or assistive tool which can overcome limitations in experimental hypothesis testing.

An in-depth summary of the following chapter is as follows:

Blood flow regulation within the microvasculature reflects a complex interaction of regulatory mechanisms and varies spatially and temporally according to conditions such as metabolism, growth, injury, and disease. Understanding the role of microvascular flow distributions across conditions is of interest to investigators spanning multiple disciplines; however, data collection within networks can be labor-intensive and challenging due to limited resolution. To overcome these experimental challenges, computational network models which can accurately simulate vascular behavior are highly beneficial. Constrained constructive optimization (CCO) is a commonly used algorithm for vascular simulation, particularly well known for its adaptability towards vascular modelling across tissues. The present work demonstrates an implementation of CCO aimed to simulate a branching arteriolar microvasculature in healthy skeletal muscle, validated against literature including comprehensive rat gluteus maximus vasculature datasets, and reviews a list of user-specified adjustable model parameters to understand how their variability affects the simulated networks. Network geometric properties, including mean element diameters, lengths, and numbers of bifurcations per order, Horton's Law ratios, and fractal dimension, demonstrate good validation once model parameters are adjusted to experimental data. This model successfully demonstrates hemodynamic properties such as Murray's Law and the network Fahraeus effect. Application of centrifugal and Strahler ordering schemes results in divergent descriptions of identical simulated networks. This work introduces a novel CCO-based model focused on generating branching skeletal muscle microvascular arteriolar networks based on

adjustable model parameters, thus making it a valuable tool for investigations into skeletal muscle microvascular structure and tissue perfusion.

1.5 References

1. **Gordan R, Gwathmey JK, Xie L-H.** Autonomic and endocrine control of cardiovascular function. *WJC* 7: 204, 2015. doi: 10.4330/wjc.v7.i4.204.
2. **Popel AS, Johnson PC.** MICROCIRCULATION AND HEMORHEOLOGY. *Annu Rev Fluid Mech* 37: 43–69, 2005. doi: 10.1146/annurev.fluid.37.042604.133933.
3. **Al Tarhuni M, Goldman D, Jackson DN.** Comprehensive *In Situ* Analysis of Arteriolar Network Geometry and Topology in Rat Gluteus Maximus Muscle. *Microcirculation* 23: 456–467, 2016. doi: 10.1111/micc.12292.
4. **Pries AR, Secomb TW, Gaehtgens P.** Relationship between structural and hemodynamic heterogeneity in microvascular networks. *American Journal of Physiology-Heart and Circulatory Physiology* 270: H545–H553, 1996. doi: 10.1152/ajpheart.1996.270.2.H545.
5. **Pries AR, Secomb TW, Gaehtgens P, Gross JF.** Blood flow in microvascular networks. Experiments and simulation. *Circ Res* 67: 826–834, 1990. doi: 10.1161/01.RES.67.4.826.
6. **Guven G, Hilty MP, Ince C.** Microcirculation: Physiology, Pathophysiology, and Clinical Application. *Blood Purif* 49: 143–150, 2020. doi: 10.1159/000503775.
7. **Halvorson BD, Bao Y, Ward AD, Goldman D, Frisbee JC.** Regulation of Skeletal Muscle Resistance Arteriolar Tone: Integration of Multiple Mechanisms. *J Vasc Res* 60: 245–272, 2023. doi: 10.1159/000533316.
8. **Chaudhry R, Miao JH, Rehman A.** Physiology, Cardiovascular [Online]. In: *StatPearls*. StatPearls Publishing <http://www.ncbi.nlm.nih.gov/books/NBK493197/> [18 Mar. 2024].
9. **Lee RM.** Morphology of cerebral arteries. *Pharmacol Ther* 66: 149–173, 1995. doi: 10.1016/0163-7258(94)00071-a.
10. **Popel A.** Network Models of Peripheral Circulation. 1987, p. 20.1-20.24.
11. **Frisbee JC, Wu F, Goodwill AG, Butcher JT, Beard DA.** Spatial heterogeneity in skeletal muscle microvascular blood flow distribution is increased in the metabolic syndrome. *American Journal of Physiology-Regulatory, Integrative and Comparative Physiology* 301: R975–R986, 2011. doi: 10.1152/ajpregu.00275.2011.
12. **Pries AR, Secomb TW.** Blood Flow in Microvascular Networks. In: *Microcirculation*. Elsevier, p. 3–36.
13. **Rahman M, Siddik AB.** Anatomy, Arterioles [Online]. In: *StatPearls*. StatPearls Publishing <http://www.ncbi.nlm.nih.gov/books/NBK555921/> [4 Jul. 2024].

14. **Poole DC, Musch TI.** Capillary-Mitochondrial Oxygen Transport in Muscle: Paradigm Shifts. *Function* 4: zqad013, 2023. doi: 10.1093/function/zqad013.
15. **Sakai T, Hosoyamada Y.** Are the precapillary sphincters and metarterioles universal components of the microcirculation? An historical review. *J Physiol Sci* 63: 319–331, 2013. doi: 10.1007/s12576-013-0274-7.
16. **Pries AR, Secomb TW.** Making Microvascular Networks Work: Angiogenesis, Remodeling, and Pruning. *Physiology* 29: 446–455, 2014. doi: 10.1152/physiol.00012.2014.
17. **Engelson ET, Skalak TC, Schmid-Schönbein GW.** The microvasculature in skeletal muscle. *Microvascular Research* 30: 29–44, 1985. doi: 10.1016/0026-2862(85)90035-4.
18. **Hill MA, Trippe KM, Li Q-X, Meininger GA.** Arteriolar arcades and pressure distribution in cremaster muscle microcirculation. *Microvascular Research* 44: 117–124, 1992. doi: 10.1016/0026-2862(92)90106-Y.
19. **Al Tarhuni M.** Comprehensive Topological, Geometric, And Hemodynamic Analysis Of The Rat Gluteus Maximus Arteriolar Networks [Online]. <https://api.semanticscholar.org/CorpusID:13821825>.
20. **Peker E.** Trifurcation of the Left Common Carotid Artery. *Pol J Radiol* 80: 376–378, 2015. doi: 10.12659/PJR.894579.
21. **Strahler AN.** Quantitative analysis of watershed geomorphology. *Eos Trans AGU* 38: 913–920, 1957. doi: 10.1029/TR038i006p00913.
22. **Horton RE.** EROSIONAL DEVELOPMENT OF STREAMS AND THEIR DRAINAGE BASINS; HYDROPHYSICAL APPROACH TO QUANTITATIVE MORPHOLOGY. *Geol Soc America Bull* 56: 275, 1945. doi: 10.1130/0016-7606(1945)56[275:EDOSAT]2.0.CO;2.
23. **Wiedeman MP.** Dimensions of Blood Vessels from Distributing Artery to Collecting Vein. *Circulation Research* 12: 375–378, 1963. doi: 10.1161/01.RES.12.4.375.
24. **Jiang ZL, Kassab GS, Fung YC.** Diameter-defined Strahler system and connectivity matrix of the pulmonary arterial tree. *Journal of Applied Physiology* 76: 882–892, 1994. doi: 10.1152/jappl.1994.76.2.882.
25. **Kassab GS, Berkley J, Fung Y-CB.** Analysis of pig's coronary arterial blood flow with detailed anatomical data. *Ann Biomed Eng* 25: 204–217, 1997. doi: 10.1007/BF02738551.

26. **Woldenberg MJ.** Quantitative Analysis of Biological and Fluvial Networks. In: *Microvascular Networks: Experimental and Theoretical Studies*. S. Karger AG, 1986, p. 12–26.
27. **Koller A, Dawant B, Liu A, Popel AS, Johnson PC.** Quantitative analysis of arteriolar network architecture in cat sartorius muscle. *American Journal of Physiology-Heart and Circulatory Physiology* 253: H154–H164, 1987. doi: 10.1152/ajpheart.1987.253.1.H154.
28. **Ellsworth ML, Liu A, Dawant B, Popel AS, Pittman RN.** Analysis of vascular pattern and dimensions in arteriolar networks of the retractor muscle in young hamsters. *Microvascular Research* 34: 168–183, 1987. doi: 10.1016/0026-2862(87)90051-3.
29. **Murray CD.** The Physiological Principle of Minimum Work: I. The Vascular System and the Cost of Blood Volume. *Proc Natl Acad Sci USA* 12: 207–214, 1926. doi: 10.1073/pnas.12.3.207.
30. **Kassab GS.** Scaling laws of vascular trees: of form and function. *American Journal of Physiology-Heart and Circulatory Physiology* 290: H894–H903, 2006. doi: 10.1152/ajpheart.00579.2005.
31. **Poiseuille 1799-1869., Royal College of Surgeons of England.** Recherches sur la force du coeur aortique [Online]. De l'impr. de Didot le jeune. <http://wellcomelibrary.org/item/b22291611>.
32. **Poiseuille JL.** *Recherches expérimentales sur le mouvement des liquides dans les tubes de très-petits diamètres*. Imprimerie Royale, 1844.
33. **Pincock C.** The derivation of Poiseuille's law: heuristic and explanatory considerations. *Synthese* 199: 11667–11687, 2021. doi: 10.1007/s11229-021-03306-1.
34. **Sutera SP, Skalak R.** The History of Poiseuille's Law. *Annu Rev Fluid Mech* 25: 1–20, 1993. doi: 10.1146/annurev.fl.25.010193.000245.
35. **Hagenbach Ed.** Ueber die Bestimmung der Zähigkeit einer Flüssigkeit durch den Ausfluss aus Röhren. *Annalen der Physik* 185: 385–426, 1860. doi: 10.1002/andp.18601850302.
36. **Secomb TW.** Blood Flow in the Microcirculation. *Annu Rev Fluid Mech* 49: 443–461, 2017. doi: 10.1146/annurev-fluid-010816-060302.
37. **Goldsmith HL, Cokelet GR, Gahtgens P.** Robin Fahraeus: evolution of his concepts in cardiovascular physiology. *American Journal of Physiology-Heart and Circulatory Physiology* 257: H1005–H1015, 1989. doi: 10.1152/ajpheart.1989.257.3.H1005.

38. **Goldsmith HL, Mason SG.** Axial Migration of Particles in Poiseuille Flow. *Nature* 190: 1095–1096, 1961. doi: 10.1038/1901095a0.
39. **Pries AR, Neuhaus D, Gaehtgens P.** Blood viscosity in tube flow: dependence on diameter and hematocrit. *American Journal of Physiology-Heart and Circulatory Physiology* 263: H1770–H1778, 1992. doi: 10.1152/ajpheart.1992.263.6.H1770.
40. **Pries AR, Ley K, Claassen M, Gaehtgens P.** Red cell distribution at microvascular bifurcations. *Microvascular Research* 38: 81–101, 1989. doi: 10.1016/0026-2862(89)90018-6.
41. **Schonberger ZG, Huang SJY, Thakkar RN, Mamone AA, Khan DI, Chow NLY, Ahmed M, Sivaram N, Bao Y, Kesavan V, Côté J, Sun C, Chhina J, Halvorson BD, Alimorad GH, Menon NJ, Goldman D, Frisbee SJ.** Assessments of Perfusion, Blood Flow, and Vascular Structure in Ambulatory Subjects: Guidance for Translational Research Scientists. *J Vasc Res* 60: 12–68, 2023. doi: 10.1159/000527765.
42. **Houben AJHM, Martens RJH, Stehouwer CDA.** Assessing Microvascular Function in Humans from a Chronic Disease Perspective. *JASN* 28: 3461–3472, 2017. doi: 10.1681/ASN.2017020157.
43. **Rizzoni D, Mengozzi A, Masi S, Agabiti Rosei C, De Ciuceis C, Virdis A.** New Noninvasive Methods to Evaluate Microvascular Structure and Function. *Hypertension* 79: 874–886, 2022. doi: 10.1161/HYPERTENSIONAHA.121.17954.
44. **Al-Khazraji BK, Novielli NM, Goldman D, Medeiros PJ, Jackson DN.** A Simple “Streak Length Method” for Quantifying and Characterizing Red Blood Cell Velocity Profiles and Blood Flow in Rat Skeletal Muscle Arterioles: Red Blood Cell Velocity Profiles in Arterioles. *Microcirculation* 19: 327–335, 2012. doi: 10.1111/j.1549-8719.2012.00165.x.
45. **Huang SJY, Wang X, Halvorson BD, Bao Y, Frisbee SJ, Frisbee JC, Goldman D.** Laser Doppler Fluximetry in Cutaneous Vasculature: Methods for Data Analyses. *J Vasc Res* : 1–15, 2024. doi: 10.1159/000538718.
46. **Fick A.** Ueber den Druck in den Blutkapillaren. *Archiv für die gesamte Physiologie des Menschen und der Tiere* 42: 482–488, 1888.
47. **Gross J, Intaglietta M, Zweifach B.** Network model of pulsatile hemodynamics in the microcirculation of the rabbit omentum. *American Journal of Physiology-Legacy Content* 226: 1117–1123, 1974. doi: 10.1152/ajplegacy.1974.226.5.1117.
48. **Pries AR, Secomb TW, Gaehtgens P.** Structure and hemodynamics of microvascular networks: heterogeneity and correlations. *American Journal of Physiology-Heart and Circulatory Physiology* 269: H1713–H1722, 1995. doi: 10.1152/ajpheart.1995.269.5.H1713.

49. **Radaelli AG, Peiró J.** On the segmentation of vascular geometries from medical images. *Numer Methods Biomed Eng* 26: 3–34, 2010. doi: 10.1002/cnm.1290.
50. **West BJ, Goldberger AL.** Physiology in fractal dimensions. *American Scientist* 75: 354–365, 1987.
51. **Gottlieb ME.** Modelling Blood Vessels: A Deterministic Method With Fractal Structure Based On Physiological Rules. In: [1990] *Proceedings of the Twelfth Annual International Conference of the IEEE Engineering in Medicine and Biology Society*. [1990] Twelfth Annual International Conference of the IEEE Engineering in Medicine and Biology Society. IEEE, p. 1386–1387.
52. **Schreiner W.** Computer generation of complex arterial tree models. *Journal of Biomedical Engineering* 15: 148–150, 1993. doi: 10.1016/0141-5425(93)90046-2.
53. **Schreiner W, Buxbaum PF.** Computer-optimization of vascular trees. *IEEE Trans Biomed Eng* 40: 482–491, 1993. doi: 10.1109/10.243413.
54. **Schreiner W, Neumann F, Neumann M, End A, Roedler SM, Aharinejad S.** The influence of optimization target selection on the structure of arterial tree models generated by constrained constructive optimization. *Journal of General Physiology* 106: 583–599, 1995. doi: 10.1085/jgp.106.4.583.
55. **Schreiner W, Neumann M, Neumann F, Roedler SM, End A, Buxbaum P, Müller MR, Spieckermann P.** The branching angles in computer-generated optimized models of arterial trees. *Journal of General Physiology* 103: 975–989, 1994. doi: 10.1085/jgp.103.6.975.
56. **Karch R, Neumann F, Neumann M, Schreiner W.** A three-dimensional model for arterial tree representation, generated by constrained constructive optimization. *Computers in Biology and Medicine* 29: 19–38, 1999. doi: 10.1016/S0010-4825(98)00045-6.
57. **Schreiner W, Neumann F, Neumann M, End A, Roedler SM.** Anatomical Variability and Functional Ability of Vascular Trees Modeled by Constrained Constructive Optimization. *Journal of Theoretical Biology* 187: 147–158, 1997. doi: 10.1006/jtbi.1997.0413.
58. **Karch R, Neumann F, Neumann M, Schreiner W.** Functional Characteristics of Optimized Arterial Tree Models Perfusing Volumes of Different Thickness and Shape. *J Vasc Res* 37: 250–264, 2000. doi: 10.1159/000025739.
59. **Schreiner W, Neumann F, Neumann M, End A, Müller MR.** Structural Quantification and Bifurcation Symmetry in Arterial Tree Models Generated by Constrained Constructive Optimization. *Journal of Theoretical Biology* 180: 161–174, 1996. doi: 10.1006/jtbi.1996.0092.

60. **Karch R, Neumann F, Podesser BK, Neumann M, Szawlowski P, Schreiner W.** Fractal Properties of Perfusion Heterogeneity in Optimized Arterial Trees. *Journal of General Physiology* 122: 307–322, 2003. doi: 10.1085/jgp.200208747.
61. **Bui AV, Manasseh R, Liffman K, Šutalo ID.** Development of optimized vascular fractal tree models using level set distance function. *Medical Engineering & Physics* 32: 790–794, 2010. doi: 10.1016/j.medengphy.2010.04.014.
62. **Schreiner W, Neumann F, Karch R, Neumann M, Roedler SM, End A.** Shear Stress Distribution in Arterial Tree Models, Generated by Constrained Constructive Optimization. *Journal of Theoretical Biology* 198: 27–45, 1999. doi: 10.1006/jtbi.1999.0898.
63. **Schreiner W, Karch R, Neumann M, Neumann F, Roedler SM, Heinze G.** Heterogeneous Perfusion is a Consequence of Uniform Shear Stress in Optimized Arterial Tree Models. *Journal of Theoretical Biology* 220: 285–301, 2003. doi: 10.1006/jtbi.2003.3136.
64. **Kopylova VS, Boronovskiy SE, Nartsissov YR.** Multiparametric topological analysis of reconstructed rat brain arterial system. *Phys Biol* 16: 056002, 2019. doi: 10.1088/1478-3975/ab2704.
65. **Linninger AA, Gould IG, Marinnan T, Hsu C-Y, Chojecki M, Alaraj A.** Cerebral Microcirculation and Oxygen Tension in the Human Secondary Cortex. *Ann Biomed Eng* 41: 2264–2284, 2013. doi: 10.1007/s10439-013-0828-0.
66. **Jaquet C, Najman L, Talbot H, Grady L, Schaap M, Spain B, Kim HJ, Vignon-Clementel I, Taylor CA.** Generation of Patient-Specific Cardiac Vascular Networks: A Hybrid Image-Based and Synthetic Geometric Model. *IEEE Trans Biomed Eng* 66: 946–955, 2019. doi: 10.1109/TBME.2018.2865667.
67. **Ii S, Kitade H, Ishida S, Imai Y, Watanabe Y, Wada S.** Multiscale modeling of human cerebrovasculature: A hybrid approach using image-based geometry and a mathematical algorithm. *PLoS Comput Biol* 16: e1007943, 2020. doi: 10.1371/journal.pcbi.1007943.
68. **Schreiner W, Karch R, Neumann M, Neumann F, Szawlowski P, Roedler S.** Optimized arterial trees supplying hollow organs. *Medical Engineering & Physics* 28: 416–429, 2006. doi: 10.1016/j.medengphy.2005.07.019.
69. **Kretowski M, Rolland Y, Bézy-Wendling J, Coatrieux J-L.** Fast algorithm for 3-D vascular tree modeling. *Computer Methods and Programs in Biomedicine* 70: 129–136, 2003. doi: 10.1016/S0169-2607(01)00200-0.
70. **Blanco PJ, de Queiroz RAB, Feijóo RA.** A computational approach to generate concurrent arterial networks in vascular territories: CONCURRENT ARTERIAL NETWORKS GENERATION IN VASCULAR TERRITORIES. *Int J Numer Meth Biomed Engng* 29: 601–614, 2013. doi: 10.1002/cnm.2547.

71. **Di Gregorio S, Fedele M, Pontone G, Corno AF, Zunino P, Vergara C, Quarteroni A.** A computational model applied to myocardial perfusion in the human heart: From large coronaries to microvasculature. *Journal of Computational Physics* 424: 109836, 2021. doi: 10.1016/j.jcp.2020.109836.
72. **Papamanolis L, Kim HJ, Jaquet C, Sinclair M, Schaap M, Danad I, van Diemen P, Knaapen P, Najman L, Talbot H, Taylor CA, Vignon-Clementel I.** Myocardial Perfusion Simulation for Coronary Artery Disease: A Coupled Patient-Specific Multiscale Model. *Ann Biomed Eng* 49: 1432–1447, 2021. doi: 10.1007/s10439-020-02681-z.
73. **Hartung G, Vesel C, Morley R, Alaraj A, Sled J, Kleinfeld D, Linninger A.** Simulations of blood as a suspension predicts a depth dependent hematocrit in the circulation throughout the cerebral cortex. *PLoS Comput Biol* 14: e1006549, 2018. doi: 10.1371/journal.pcbi.1006549.
74. **Talou GDM, Safaei S, Hunter PJ, Blanco PJ.** Adaptive constrained constructive optimisation for complex vascularisation processes. *Sci Rep* 11: 6180, 2021. doi: 10.1038/s41598-021-85434-9.
75. **Pries AR, Schonfeld D, Gaehtgens P, Kiani MF, Cokelet GR.** Diameter variability and microvascular flow resistance. *American Journal of Physiology-Heart and Circulatory Physiology* 272: H2716–H2725, 1997. doi: 10.1152/ajpheart.1997.272.6.H2716.
76. **Mayooran T, Light E.** Applying the successive over-relaxation method to a real world problems. *American Journal of Applied Mathematics and Statistics* 4: 113–117, 2016.
77. **Thomas B, Sumam KS.** Blood Flow in Human Arterial System-A Review. *Procedia Technology* 24: 339–346, 2016. doi: 10.1016/j.protcy.2016.05.045.
78. **Gompper G, Fedosov DA.** Modeling microcirculatory blood flow: current state and future perspectives. *WIREs Mechanisms of Disease* 8: 157–168, 2016. doi: 10.1002/wsbm.1326.
79. **Fenton BM, Wilson DW, Cokelet GR.** Analysis of the effects of measured white blood cell entrance times on hemodynamics in a computer model of a microvascular bed. *Pflügers Arch* 403: 396–401, 1985. doi: 10.1007/BF00589252.
80. **Schmid-Schönbein GW, Skalak R, Usami S, Chien S.** Cell distribution in capillary networks. *Microvascular Research* 19: 18–44, 1980. doi: 10.1016/0026-2862(80)90082-5.

Chapter 2

2 A Constrained Constructive Optimization Model of Branching Arteriolar Networks in Rat Skeletal Muscle

The contents of this chapter have been published in *Journal of Applied Physiology* in May 2024.

2.1 Introduction

The role of the circulatory system is to effectively deliver and distribute blood throughout the body. Arteries and arterioles are an essential component of the process as they deliver oxygen and nutrients to the organs and tissues and link to capillaries, which act as sites of resource exchange within tissue. The degree of active tone in the arterioles, defined by the state of constriction of vascular smooth muscle within the vessel, is the integrated result of regulatory mechanisms such as local oxygen tension, intravascular pressure, autonomic nervous stimuli, wall shear stress, etc. (1), and will cause constant changes to arteriolar diameter, which greatly influence perfusion resistance (2), and thus, the distribution of blood within the tissue or organs under investigation. Vascular remodeling and changes in capillary density are also used to influence blood supply; however, these mechanisms are not relevant for moment-to-moment control of blood flow distribution.

Disease and disease risk is often associated with impaired or disturbed blood flow distribution both to and within tissues and organs, which manifests as impaired function. Due to the importance of arteriolar diameter and vessel network structure on blood flow regulation (2–4), investigations to understand blood flow distribution under

pathophysiologic conditions necessitate models for the relevant vascular networks. While models can be, and have been, based on data acquired from experimental procedures, arteriolar networks have a range of vessel dimensions, and it can be unrealistic to acquire sufficiently accurate data across all necessary levels of resolution using standard clinical and experimental approaches. As a result, there is potential for large amounts of important data to be excluded in experimentally acquired models, limiting their likeness to real vasculature. For tissues such as skeletal muscle, geometric and topological data of arteriolar networks have been reported (3, 5–8), however they are often limited to small microvascular segments with a narrow range of arteriolar diameters (typically 10–40 μm).

Computational models have alternatively been built using mathematical algorithms which aim to approximate the real world physical and physiological characteristics of the networks under investigation. For example, some studies have attempted to use computational modelling to address sections of missing vascular data in experimental models, attaching computationally generated data to extend existing vasculature (9–11). Some studies attempt to generate realistic vascular networks without building upon pre-existing experimental data. Various methods have been proposed for such models, such as using simplified topologies (12), fractals (13), or a space-filling method (14–16).

Theoretical models based on simplified topologies attempt to represent vascular networks as a chain of elements in series, with each element representing a vessel (12). While such approaches may be sufficient for the statistical approximation of a vascular network, actual networks are heterogenous in structure which may play a significant role in vasculature function by causing flow heterogeneity (4). Models based on fractal patterns also bear a similar problem: fractal models are built based on the observation that branching

vessel networks possess the notable repeating pattern of parent vessels splitting into two daughter vessels at each bifurcation, irrespective of diameter; branching networks possess a degree of self-similarity at different scales which gives them fractal properties (17). Fractal models attempt to generate networks based on the concept of self-similarity by repeating fixed patterns of vessel connectivity, but often result in networks with geometries which are almost impossible to find in nature (18, 19).

Space-filling methods attempt to emulate the way that real vasculature grows through computational means. Algorithms for space-filling have been proposed based on whether real vasculature is hypothesized to grow based on avoiding existing vasculature (16) or filling in space as much as possible (15). By implementing a series of constraints on how the network can grow and adding an optimization target that aligns with what real vasculature is hypothesized to target, the vascular networks can be forced to grow within a space in the pre-specified “optimal” way, naturally resulting in heterogenous, realistic networks.

The most prevalent space-filling method is known as constrained constructive optimization (CCO), which sequentially generates and attaches vessels to existing vasculature, filling in the tissue space based on the minimization of some select parameter hypothesized to be costly in the process of microvascular vessel growth, such as blood volume (15). As a result, CCO constructs branching networks which obey bifurcation rules, such as fractal scaling and flow conservation, while incorporating geometric and structural optimizations and ensuring uniform blood perfusion in a designated area. CCO has been used to study network properties relating to anatomical variability (20), fractal properties (14), and shear stress distribution (21), among others. Given this, using the CCO approach

has been demonstrated to provide for a flexible method of generating vessel networks which can be readily adapted to various desired outcomes.

Past usages of computational models have frequently been catered towards the exploration of specific physiologies and conditions. Due to difficulties in acquiring experimental models, it would be beneficial for investigators to have access to a customizable computational model which can generate realistic vasculatures for various physiologies of interest, but such a product has been rarely explored. Current attempts to address such a demand have not been well validated against experimental data and have not been made accessible to those who are unable to develop models on their own.

An overarching aim of the present work is to develop a CCO-based model which can generate realistic arteriolar networks for a range of tissues, depending on user-adjustable parameters such as the tissue's geometry, the network density and size, etc., which are experimentally informed to be appropriate for the specific tissue. While current efforts to utilize CCO tend to occur at the macrovascular scale, the present work will implement CCO at the microvascular level. Microvascular networks are commonly studied in skeletal muscle due to the ease of access and flat tissue geometry of some skeletal muscle preparations. This enables data collection with a high degree of accuracy, as imaging modalities such as intravital video microscopy (IVVM) do not have to penetrate the tissue very deeply to reach the vessels. The microvasculature is also an area of importance because it is the location of blood flow-tissue exchange, and hence is highly sensitive to changes in the physiological state such as disease. Hence, as a starting point for the overarching aim, the present work showcases an implementation of CCO aimed at simulating branching arteriolar networks within skeletal muscle based on data from

microvascular networks within healthy rat gluteus maximus tissue. The model will be validated to demonstrate whether it can generate networks which are closely comparable to arteriolar microvascular networks within skeletal muscle tissue; structural and hemodynamic properties for the simulated networks will be comprehensively validated according to values published in literature and previously collected experimental data (22, 23) which, to date, is one of the most detailed analyses of geometric and topological structure of arteriolar networks within rat skeletal muscle. Model parameters will be further explored to evaluate their impact on the geometric and hemodynamic properties of the generated networks, and to understand the adaptability of the generated networks for modelling microvasculature in various skeletal muscle tissues.

2.2 Methods

Rat Gluteus Maximus Muscle Vascular Data: The vascular data used to validate the model was collected in a previous study (22), in collaboration with an affiliated group at Western University. Vascular networks within the gluteus maximus muscle of Sprague-Dawley rats ($n=8$; 8-9 weeks of age; mass = 303 ± 15 g) were measured in situ under control conditions (i.e., no imposed intervention) using IVVM over eight arteriolar orders. A photomontage composed of ~ 500 overlapping frames, with a total microvascular area of ~ 4 cm², was constructed from each animal using MATLAB (MathWorks Inc., Natick, MA, USA; RRID:SCR_001622). The hemodynamic and geometric properties of the intramuscular vasculature were analyzed from the IVVM photomontage: vessel segment lengths, vessel segment diameters, and number of vessels per vascular order were measured using ImageJ (RRID:SCR_003070) (24). Additionally, the overall fractal dimension for

multiple networks was analyzed using single line tracings of the IVVM networks using FracLac (25), a toolbox in ImageJ. Full details on the data collection procedure for the networks' geometric properties are described in (22).

To collect hemodynamic data, fluorescent red blood cells were injected into the rats via the jugular vein, and fluorescent images were collected at 5-20 millisecond exposure times, higher for larger, and lower for smaller arterioles. As such, fluorescing red blood cells formed short streaks in the images. Based on the number of red blood cells spanning each arteriolar lumen, the lumens were split into "lanes". Multiple streak measurements were made across the lumen within each lane using ImageJ, and the average red blood cell velocity in each lane was plotted to create a velocity distribution profile for each vessel segment. Based on the velocity distribution profile and red blood cell dimensions, red blood cell flow and flow through the cell-free layer was calculated in MATLAB (R2010a, The MathworksTM, Inc.). Full details on data collection and processing are described in (23).

Model Algorithm: The model was built to generate branching arteriolar tree networks grown in a circular 2D tissue space, which was considered to represent a portion of the gluteus maximus area. Since the gluteus maximus is a relatively thin muscle, its arteriolar vasculature has previously been considered two-dimensional in experiment-based reconstructions (22, 23); here too, a 2D approach to applying the CCO network construction algorithm to the GM was determined to be appropriate for the present study. The vessels of the network were modeled as straight cylindrical tubes, a commonly implemented approximation for the vessel's geometry in microvascular networks (26).

For the model to produce experimentally accurate vascular networks, some of the key initial parameters were specified based on previously collected vascular and hemodynamic data from the rat gluteus maximus muscle (22, 23). Q_{perf} , defined as the total flow within each terminal arteriole, was set to 1.2×10^{-7} mL/s by assuming a terminal arteriole of approximately 9 microns in diameter and using the diameter-flow relation in (23). A_{perf} , the tissue area perfused per terminal arteriole, was set to 3.6×10^{-3} cm² by assuming the area of the arteriolar network in (22) was approximately 2cm² and the largest arteriole was approximately 100 microns in diameter. Using the diameter-flow relation in (23), dividing total flow by terminal arteriole flow gave the number of terminal arterioles, which was used to calculate A_{perf} . dP_{tot} , the pressure gradient from network inlet to outlet of each terminal arteriole, was set to 8050 dyne/cm² (6 mmHg) by assuming initial arteriole length (L) and diameter (D) of 300 and 9 microns, respectively, and a viscosity of $\mu = 3.6$ cP, and applying the Poiseuille pressure-flow relation, $dP_{tot} = 128\mu L Q_{perf} / \pi D^4$. Initial input for the Murray's law exponent γ , which characterizes the relationship between diameter and blood flow, was set to 2.6 (23). Unless otherwise specified, all networks generated within this study used these parameters by default. Variable names and definitions in the present work are summarized in Table 1.

Table 1: Summary of Model Parameter Variables and their definitions.

Variable Names	Default Value	Definition
<i>Nbif</i>	N/A	The number of bifurcations in the generated network.
<i>Qperf</i>	0.12 nL/s	Total flow within each terminal arteriole
<i>Aperf</i>	0.0036 cm ²	Total tissue area perfused per terminal arteriole
γ	2.6	The Murray's law exponent, which characterizes the power law relationship between diameter and blood flow
<i>expVal</i>	0 (off)	A percentage value, where any daughter vessel with a diameter which is less than this percentage of the parent's diameter is ignored.

The algorithm used to implement CCO for a healthy vascular network within the flat circular tissue can be described as follows:

1. Specify a *Nbif* value. This is the number of bifurcations desired within the network.
2. Specify the radius of the flat circular tissue which the network will be growing within. The area of this circle will be equivalent to *Aperf* initially, as only the inlet arteriole will be initially present.

3. Specify the starting location where the inlet arteriole of the network should be placed. Randomly select a point in tissue space (which theoretically, requires blood perfusion) and connect a terminal arteriole from the starting location to the point.
4. Repeat the below steps until the vascular network has sufficiently filled in the tissue space (i.e., the desired $Nbif$ is reached):
 - a. Increase the tissue space size by $Aperf$ to accommodate the perfusion area of one more terminal arteriole.
 - b. Randomly select a point within the tissue space which requires blood perfusion.
 - c. Connect a new vessel from the existing vascular network to that point; the new vessel should bifurcate from the vessel that will yield a minimum total network blood volume.
5. Optimize the bifurcation angles between the existing vascular network and the newly added vessel to further reduce total blood volume.

For further clarity, Figure 4 provides a visual of the algorithm in a step-by-step fashion. The random selection of points in step 3 and 4b was implemented for the purpose of generating networks which are different in each run, and yet statistically similar, provided no other parameters are changed. Ideally, such a procedure would be able to reflect the slight variations in growth found in real life vasculatures of the same physiology. Regarding the tissue space size $Atot = (Nbif + 1) \cdot Aperf$, where $Nbif$ is the number of bifurcations, the tissue will continue to grow as bifurcations are added, but the relative rate of growth ($1/Nbif$) will approach zero as the number of bifurcations becomes large.

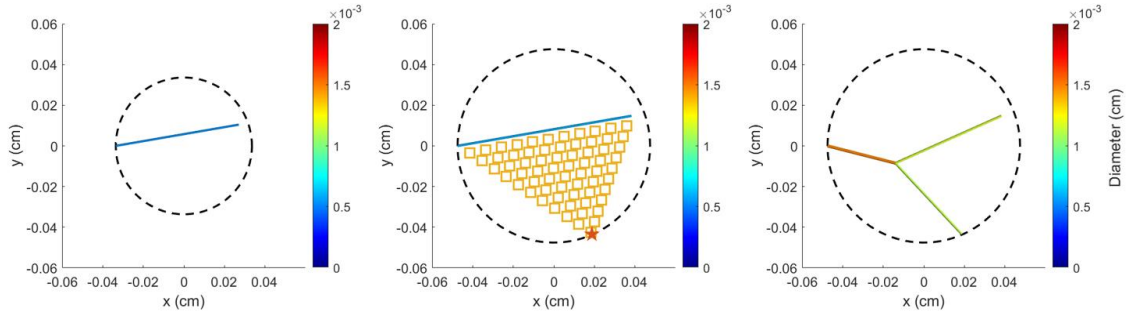


Figure 4. A step-by-step diagram of the model algorithm, as described in the methods. The dotted circle is the tissue area within which the network is allowed to grow. The vessels are represented by lines, colored by diameter in cm. Panel a) represents steps 1, 2 and 3 of the algorithm. Panel b) represents step 4. Step 4a is depicted via the increase in size for the dotted circle from the previous panel, step 4b is depicted by the red star, which represents the randomly chosen end point for the newly added segment, and step 4c is depicted via the colored squares, which are potential bifurcation points tested across space between each vessel and the red star. Panel c) represents the resulting optimized bifurcation in step 5, once the optimal bifurcation point is chosen from step 4c and the vessels are connected accordingly, after which there is a return to step 4a to further expand the network.

Total network blood volume was chosen as the constrained cost function under the assumption that blood is an expensive resource that the body should aim to preserve (19). Each calculation of blood volume required updating the radii of the existing vessels of the network for each additional vessel added. The calculation of radii was performed following a two-step process: First, for some initial estimate of radii in each vessel in the network, the corresponding blood flow was solved using either a single linear inversion (constant viscosity) or following the iterative network flow simulation method (diameter- and hematocrit-dependent viscosity) described by Pries et al., 1990 (27) and previously

implemented by our group (28, 29) (note that the Pries et al. model implements conservation of both blood flow and red cell volume flow at each bifurcation). Second, given the pressure values from the flow calculation, the diameter values of all terminal vessels were adjusted such that their blood flow matched Q_{perf} , and the diameters in the rest of the network were recalculated up to the inlet vessel by applying Murray's law at each bifurcation. This two-step process was repeated until satisfactory convergence of diameter values was achieved, which typically occurred in 3-5 iterations.

While blood typically behaves as a homogenous fluid, on the microvascular scale, blood tends to behave as a two-phase fluid due to the differing properties of plasma and red blood cells (27). To test the impact of blood's two-phase nature on the properties of the network model, the networks were generated with fixed viscosity of $0.036 \text{ dyne}\cdot\text{s}/\text{cm}^2$ for blood (30), to simulate blood as a single-phase fluid, as well as with variable blood viscosity for each vessel, to simulate blood as a two-phase fluid (in which each vessel may have a different proportion of plasma and red blood cells). The resulting single-phase and two-phase flow-derived networks were compared after generation based on their geometric and topological statistics. In addition to targeting $Q_{perf} = 0.12 \text{ nL/s}$ of blood flow at the terminal vessels for both single-phased and two-phased networks, an alternative target was set under the two-phased assumption based on fixing red blood cell flow in terminal arterioles to $0.12 \text{ nL/s} * 0.4 = 0.064 \text{ nL/s}$, assuming a discharge hematocrit of 0.4 (27). This alternative target was to evaluate whether a red blood cell target would generate networks which are more similar to real vasculature, assuming tissues prioritize red blood cells within their received blood flow.

To fully fill out the tissue space and prevent the intersection of vessels, vessels were restricted from growing within a certain distance of other vessels, following suggestions from Schreiner & Buxbaum 1993 (31). If a vessel is added such that it is within a certain distance to another already existing vessel, then it is discarded and point 2b) must be resampled until the vessel is acceptably distal. This distance was set to $d_{thresh} = \sqrt{\pi r^2 / n_{term}}$, where r is the radius of the tissue space and n_{term} is the number of terminal vessels within the vasculature. If a suitable vessel cannot be found after 50 attempts of resampling point 2b), then the acceptable distance is scaled down via $d_{thresh} = d_{thresh} * 0.9$. This cycle repeats until a suitable vessel is found.

A few changes were made to shorten the computation time. Instead of testing connections to every single vessel of the existing vasculature in step 2c), to find the vessel that yields a minimum total blood volume, only the 12 vessels closest to the point in 2b) were tested. Additionally, the optimization of bifurcation angles was performed by finding the discrete point in the triangular space formed by the vessel chosen in 2c) and the point in 2b) which yields a minimum blood volume; only 66 points were tested within this triangular space, instead of using a higher resolution. These assumptions minimally impacted the resulting networks compared to when generated without.

Certain experimental studies do not include vessels sprouting from extremely asymmetric bifurcations due to challenges in collecting the data, such as limitations in imaging resolution. To better simulate such experimental conditions, in which the published experimental data may truly be representing an incomplete network, a percentage value $expVal$ was applied to the model such that any daughter vessel with a

diameter which is less than *expVal* percent of the parent's diameter is ignored. The percentage value is adjustable and was used to fit the model's geometric statistics to that of previously published experimental data. Unless the *expVal* value is specified, the model otherwise has this feature turned off, and presents the complete generated network without removal of any vessels. Figure 5 demonstrates an example of how increasing *expVal* affects the resulting network by removing decreasingly asymmetric bifurcations.

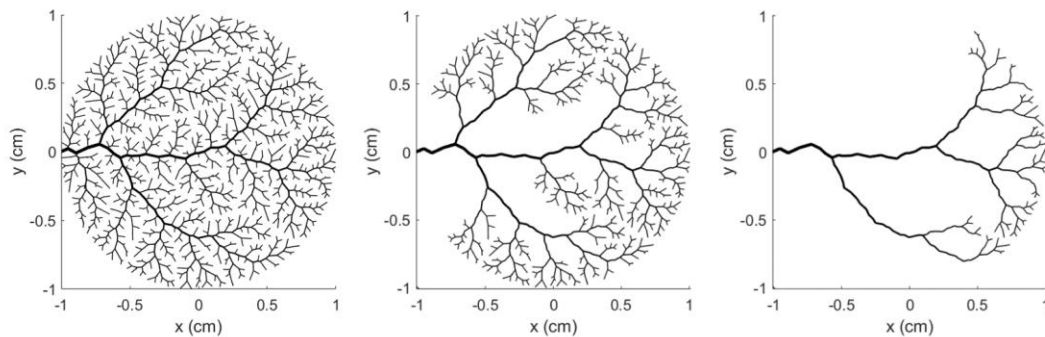


Figure 5. An example of how increasing *expVal* from a) 0% (i.e., the complete network), to b) 40% and c) 60% affects a generated network of size 900 bifurcations.

Calculation of Geometric and Hemodynamic Statistics:

Calculation of all geometrical and hemodynamic statistics for the generated networks was performed in MATLAB, save for fractal dimension. MATLAB was also used to label all vessels within the network according to Strahler's order, a purely topological, centripetal ordering scheme, using methods from Koller et al., 1987 (5).

Centrifugal order, another standardly used ordering scheme (3), was also calculated for the networks to facilitate comparisons to different datasets within the literature. To define the difference between the two ordering schemes: in Strahler's order, order 1 is assigned to terminal arterioles. Moving from the terminal arterioles to the inlet vessel, when two vessels of the same order join, the order of the parent is increased by one. If two vessels of different orders join, the parent is designated the higher of the two orders. In contrast, centrifugal order assigns order 1 to the inlet vessel. Moving from the inlet vessel to the terminal arterioles, if either or both daughters have a diameter less than 80% of the parent, or if the daughters form a bifurcation angle greater than 30° , the order of the daughters are increased by one.

Statistics were calculated based on the definition of "elements and segments" (32, 33), in which each unbranched vessel is called a "segment", and consecutive segments of the same order constitute one element. It is with the concept of segments and elements that the intuitive idea of a single major vessel with multiple smaller offshoots (one element with several different elements connected to it) was conceptualized. As a visual example, Figure 6 illustrates how Strahler's order was assigned to each "segment" within a sample network, and how consecutive "segments" of the same order compose one "element". The definition of elements and segments remained the same if centrifugal ordering was used instead, resulting in alternative interpretations based on ordering scheme of which segments compose an element.

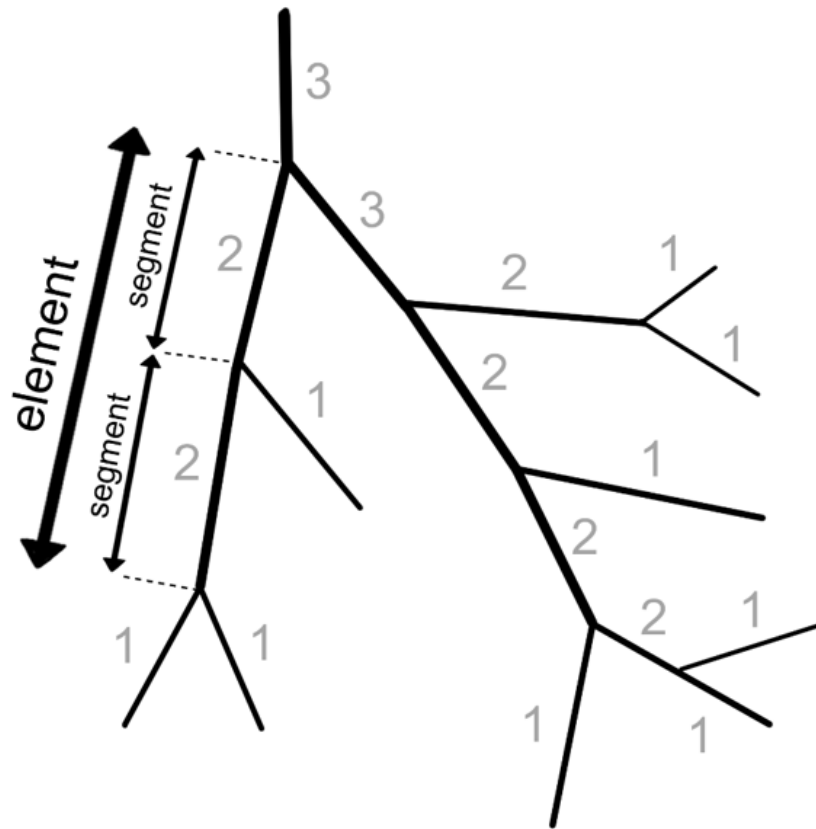


Figure 6. A schematic representation of the labeling convention for arteriolar networks in the present study based on Strahler's order. Strahler's order begins with order 1 at the terminal vessels, where the diameter is the smallest, and increases moving upwards towards the inlet arteriole, depending on if two daughters of the same order coincide at a bifurcation (in which the parent order will increase), or if two daughters of different orders coincide (in which the greater order number will persist to the parent vessel). Segments and elements are labelled, where connecting segments must have the same order number to be considered an element.

Fractal dimension has often been applied to characterizing vascular networks, as the repeating branching pattern of parent and daughter vessels has previously been

identified as fractal in nature (17). The CCO-based model introduced in the present study was built to follow the repeating branching pattern, and thus, is also fractal in nature. The FracLac toolbox (25) in ImageJ (24) was used to calculate the fractal dimension of the generated networks, as done in previous work (22). By saving the generated networks as images, the toolbox was able to scan the network image using a hull and circle technique, wherein the software calculates statistics for the tissue geometry's convex hull and minimum bounding circle, to characterize the circular geometry of the tissue. The box counting method was used to calculate the fractal dimension of the generated network, by generating boxes of varying sizes and finding the slope of the linear fit between the logarithm of the number of boxes containing a segment of the network and the logarithm of the box sizes.

Validation of Geometric and Hemodynamic Properties:

The model was primarily validated via comparison to previously collected vasculature data from the rat gluteus maximus skeletal muscle (22, 23), as it provides a highly comprehensive overview of geometric and hemodynamic properties from the same microvascular data. However, the model was also compared to multiple other skeletal muscle datasets within the literature (3, 5) to overcome experimental limitations and inconsistencies between data collection and data processing procedures. Within this study, the model was considered validated against experimental data if it 1) satisfied generally observed properties including being fractal and obeyed Horton's law and Murray's law, and 2) showed potential to match geometric and hemodynamic properties (e.g., fractal dimension and Murray's law exponent) in several specific muscles when model parameters are adjusted. As certain model inputs (such as domain geometry) are not adjusted, we do

not expect to exactly match network properties in the muscles considered. In addition, as noted, there are issues with available datasets (e.g., those motivating use of *expVal*) that make exact matching challenging. To validate the hemodynamic accuracy of our constructed networks, properties were chosen (Murray's law exponent and the network Fahraeus effect, described below) that have been reported in the literature and represent the integrated hemodynamic behavior of microvascular networks, since individual hemodynamic parameters (e.g., flow or hematocrit in a certain size vessel) are highly variable, even within a given set of experiments or single network.

To understand the geometrical features of the model and the difference between the Strahler's and centrifugal ordering schemes, the distribution of element diameter and length was evaluated. The distributions of the geometric properties were related to the rat gluteus maximus microvasculature (22). From those same elements, the mean diameter, length, and number of elements per order were calculated and plotted for both ordering schemes. To explore the flexibility of the model, adjustments were made to model parameters (e.g., *Nbif* and *expVal*) to match the resulting mean diameter, length, and number of elements per order to experimental values from previously collected microvascular data within the rat gluteus maximus muscle (22), along with other skeletal muscle datasets from the literature.

Horton's Law: Past experimental studies have demonstrated that a power law relationship exists between Strahler's order and diameter, length, and number of elements – this relationship is known as Horton's Law (34). To explore whether the model displays Horton's law, the strength of a linear fit between the log transform of mean diameter, length, and number of elements per Strahler and centrifugal order was evaluated.

Due to the linear relationship between geometric features, the slopes of the linear fits have also been used to describe the geometric properties of networks. The slope values are referred to as Horton's ratios, or diameter, length, and bifurcation ratios, which characterize the relative proportion of diameter, length, and number of elements between each successive and previous order. Due to variations in how past studies have attempted to quantify the ratios (3, 5), three methods of calculating the ratios have been presented. Method 1 consisted of finding the mean number, length, and diameter of vessels per Strahler's order from vessels accumulated from all five networks and applying a linear regression to the logarithm of those means. The ratio values were determined by the slope of the regression lines. Method 2 consisted of finding the mean number, length, and diameter of vessels per Strahler's order for vessels within each individual network, calculating ratios based on the slope of the linear fit to the logarithm of the means from each of those networks, and averaging the calculated ratios from all networks. Method 3 consisted of finding the mean number, length, and diameter of vessels per Strahler's order for each individual network, averaging the means across all networks, and finding the ratios based on the slope of the linear fit to the logarithm of the averaged means. Once the model ratio values were calculated based on these three methods, a review of Horton's law ratio values in previously published datasets was performed to enable comparison and validation.

Murray's Law: Like Horton's law, past experimental studies have demonstrated that a power law relationship exists between flow and diameter, known as Murray's Law (35). The Murray's law exponent typically ranges between approximately 2 and 4, depending on the site of flow (36). The exponent value was calculated based on the log

transforms of diameter and blood flow within all segments of multiple networks when fitted with a linear regression; since vessel length does not affect the Murray's law exponent, the calculation of elements was not necessary. Segments were used instead of elements to avoid biases relating to how ordering scheme affects element diameter, which is calculated based on the average diameter of the segments composing it. The Murray's law exponent value calculated from generated model networks was compared to the measured Murray's law exponent from vasculature within rat skeletal muscle (23).

Fahraeus Effect: The Fahraeus effect refers to the decrease of tube (volume-averaged) hematocrit, given fixed discharge (flow-averaged or 'reservoir') hematocrit, as vessel diameters decrease from approximately 300 to 10 microns. This occurs in single vessels, due to red cells being excluded from the plasma layer near the vessel wall and having a higher velocity than blood as a whole, and is not related to microvascular network properties. The *network* Fahraeus effect, whose origin is the unequal distribution of red cells and plasma at diverging bifurcations ('plasma skimming'), refers to the decrease in average discharge hematocrit in a network as diameter decreases over multiple generations, which leads to decreases in tube hematocrit beyond those predicted by the standard Fahraeus effect. The Fahraeus effect is incorporated into the two-phase blood flow model used in the present work, as is a description of plasma skimming. To verify that the model can simulate the network Fahraeus effect, which requires both plasma skimming and a suitable sequence of bifurcations in the network, discharge and tube hematocrits for segments within multiple networks were calculated and plotted versus segment diameter. Note that there are also observed reverse Fahraeus and reverse network Fahraeus effects when vessel diameters are around 10 μ m and smaller, due to the thinning of the plasma

layer (37). In the model, during the process of calculating each vessel's radius based on optimizing total network blood volume, discharge and tube hematocrit results were generated for cases that used the two-phase flow simulation (27).

Exploration of Model Properties:

To explore whether assumptions of blood as a single-phase or two-phase fluid affects the geometric properties of the model, networks were generated for each of three phase cases outlined in the model algorithm: 1) assuming blood is a single-phase fluid in which constant blood flow is maintained at the terminal arterioles, 2) assuming blood is a two-phase fluid in which constant blood flow is maintained at the terminal arterioles, and 3) assuming blood is a two-phase fluid in which constant red blood cell flow is maintained at the terminal arterioles. Case 1 may be performed by using the previously mentioned simple linear inversion method (constant viscosity) of calculating vessel radii and optimizing for Q_{perf} , whereas cases 2 and 3 rely on the iterative network flow simulation method (diameter- and hematocrit-dependent viscosity) suggested by Pries et al., 1990 (27) – with the difference of optimizing for Q_{perf} (case 2) vs. red blood cell flow (case 3). Differences in geometric properties between the cases were analyzed based on the mean and standard deviation of diameter, length, and number of elements per order, the Horton's ratios, and fractal dimension. Differences in hemodynamic properties were analyzed based on the Murray's law exponent and tube and discharge hematocrit per order.

To explore the relationship between model properties and the geometric statistics of the generated networks, changes in the diameter, length, and bifurcation ratios was explored with five networks generated under three varying cases: 1) 100 bifurcations with

varying Murray's law exponent γ , 2) 100 bifurcations with varying the tissue area perfused by each terminal arteriole in the network A_{perf} , and 3) 100 bifurcations with varying amount of blood flowing through the terminal vessels of the network Q_{perf} . The Horton's ratios were calculated based on method 2, finding the average of the linear regressions on diameter, length, and number of elements per order. Values are calculated as the ratios \pm the 95% confidence interval, with the assumption that cases with overlapping confidence intervals demonstrate insignificant differences.

To explore the fractal properties of the generated networks over varying levels of magnification, i.e., the fractal dimension of the entire network vs. smaller, local regions of similar vessel sizes, the fractal dimension was calculated in ImageJ using an increasing number of boxes and averaged. To understand how model properties affect the fractal dimension of the generated networks, fractal dimension values were calculated for networks of varying number of bifurcations N_{bif} , for networks growing with varying terminal arteriole perfusion areas A_{perf} , for varying amounts of blood flow maintained at the terminal vessels of the networks Q_{perf} , for varying percentage values of $expVal$, and for varying initial Murray's law exponents γ . Comparisons of resulting fractal dimension values were made to published fractal dimension values for the rat gluteus maximus microvasculature (22), and observations were made relating to which model parameters significantly impact fractal dimension and yield the best validation to the experimental data.

2.3 Results

To note: in investigating the multi-phase nature of blood, networks which were generated under 3 different cases, assuming blood is case 1) a single-phase fluid with a constant amount of flow maintained at terminal vessels, case 2) a two-phase fluid with a constant amount of flow maintained at terminal vessels, and case 3) a two-phase fluid with a constant amount of red blood cell flow maintained at terminal vessels, showed negligible differences in geometric statistics (mean diameter, length, and number of elements per order, Horton's ratios, and the fractal dimension in Figure 7 and 8). Though cases 2 and 3 enabled the prediction of hematocrit in all vessels, unlike in case 1, differences in hemodynamic properties between cases 2 and 3 were also negligible (Figure 9). Since considering blood as a multi-phase fluid does not seem to significantly impact the geometric properties of generated networks, for brevity, further results regarding the networks' geometric properties have only been produced with the assumption that blood is a single-phase fluid (case 1). Further results regarding the networks' hemodynamic properties (e.g., network Fahraeus effect) have been produced with the assumption that blood is a two-phase fluid, with blood flow maintained at the terminal vessels (case 2).

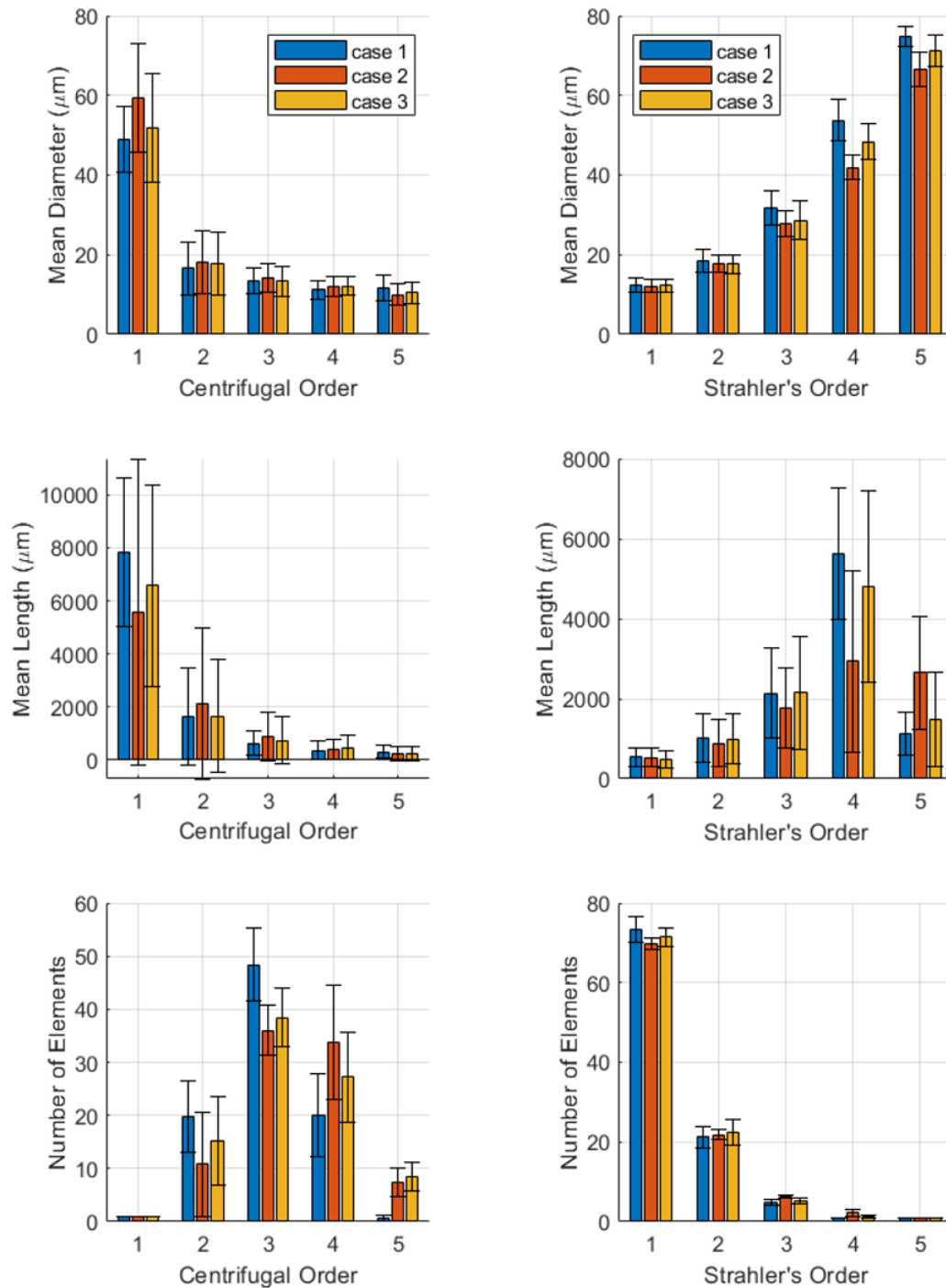


Figure 7. Mean and standard deviation of diameter, length, and number of bifurcations N_{bif} per Strahler's and centrifugal order for five networks of size 100 bifurcations generated for the 3 blood flow cases: case 1) a single-phase fluid with a constant amount

of flow maintained at terminal vessels colored in blue, case 2) a two-phase fluid with a constant amount of flow maintained at terminal vessels colored in red, and case 3) a two-phase fluid with a constant amount of red blood cell flow maintained at terminal vessels colored in yellow. Error bars represent the plus minus standard deviation per order.

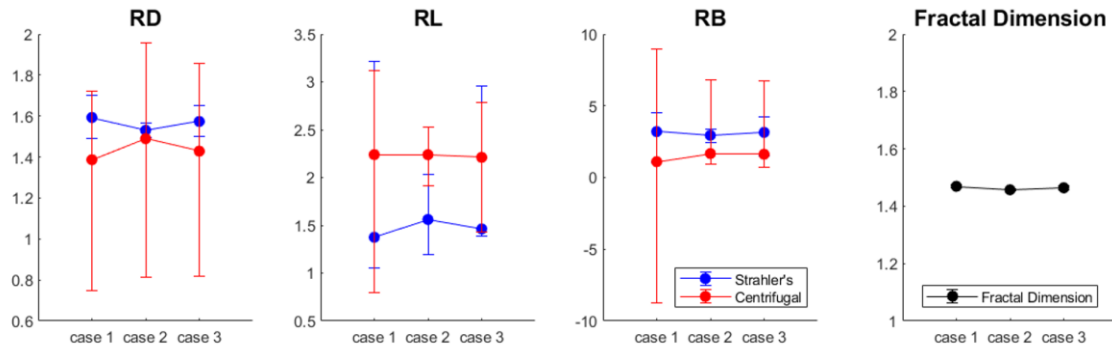


Figure 8. In panels a-c) the mean \pm 95% confidence interval of the Horton's Law ratios and in panel d) mean \pm standard deviation of fractal dimension across five 200-bifurcation networks generated for the 3 flow cases, case 1) a single-phased fluid with a constant amount of blood flow maintained at terminal vessels, case 2) a two-phased fluid with a constant amount of blood flow maintained at terminal vessels, and case 3) a two-phased fluid with a constant amount of red blood cell flow maintained at terminal vessels. The ordering schemes are colored blue for Strahler's and red for centrifugal, black for fractal dimension.

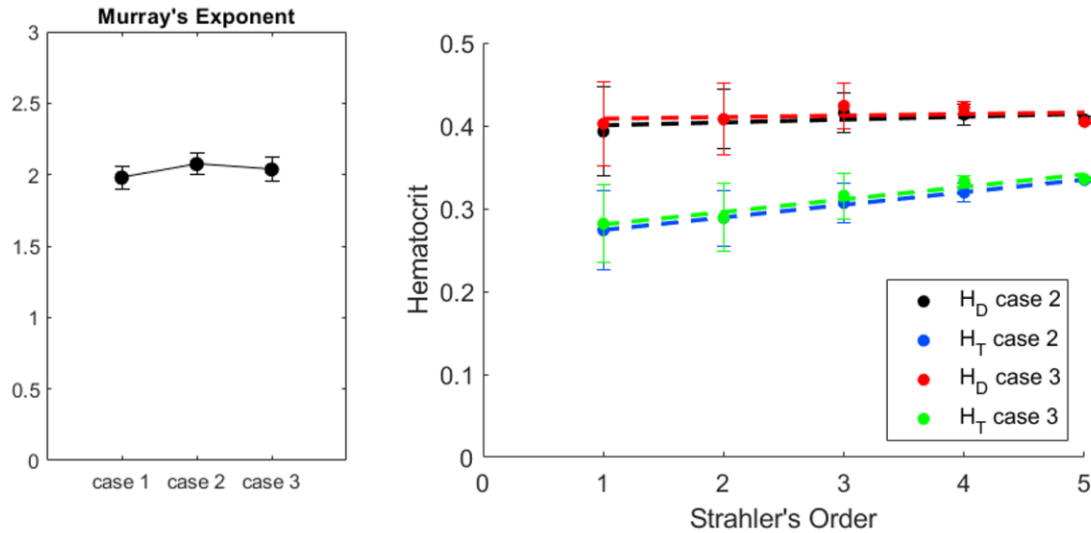


Figure 9. Hemodynamic properties tested between the three blood flow cases, calculated over five networks of 100 bifurcations per case. On the left, is the Murray's law exponent plotted as mean \pm the 95% confidence interval. On the right is the hematocrit per Strahler's order: case 2 is represented as black for discharge hematocrit and blue for tube hematocrit, case 3 is represented as red for discharge hematocrit, and green for tube hematocrit. A linear fit has been applied to the hematocrit values per order, represented by the dotted line, and the error bars represent the standard deviation.

Figures 10 and 11 are presented to aid in understanding the model's generated network outputs and the categorization of the vessels within for further hemodynamic and geometric statistical analyses. To provide a visual example of what the typical generated network looks like, Figure 10 presents a network generated using the CCO-based algorithm, grown to a total of 900 bifurcations (or 901 terminal vessels), with vessels colored by diameter. The generated vascular tree structure filling the dotted circle, which signifies the perfusable tissue area, is similar to many vascular trees observed within physiology. To clarify the difference between centrifugal and Strahler's ordering schemes,

Figure 11 demonstrates a 100-bifurcation network being ordered using both centrifugal and Strahler's ordering schemes, with the resulting element numbers labelled. Despite the same network being plotted, segment order and element numbering differ greatly between ordering schemes.

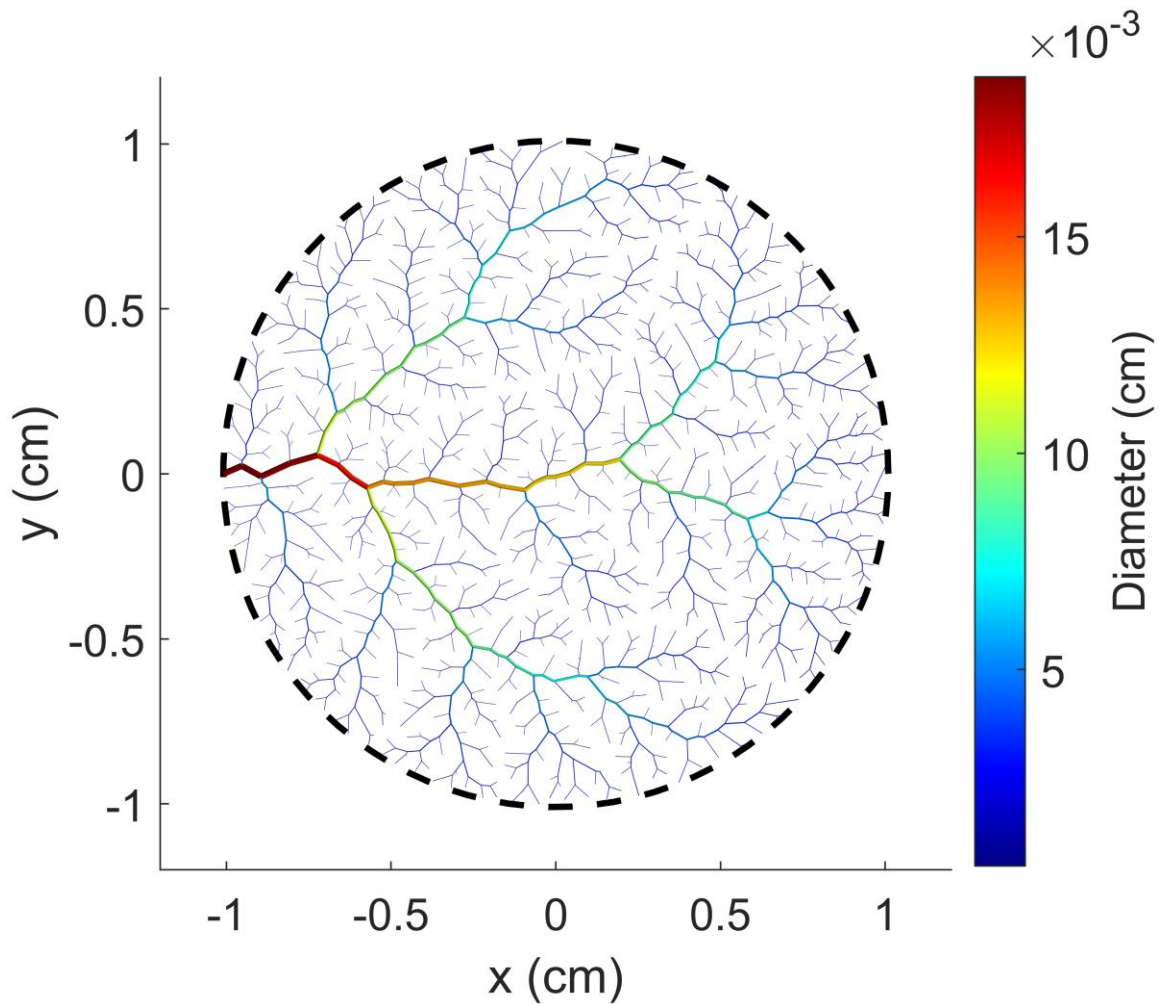


Figure 10. An example generated network, with 900 bifurcations, grown in a 2cm diameter circular flat tissue. Vessels colored by diameter (cm). Total blood volume is 6.89×10^{-4} mL.

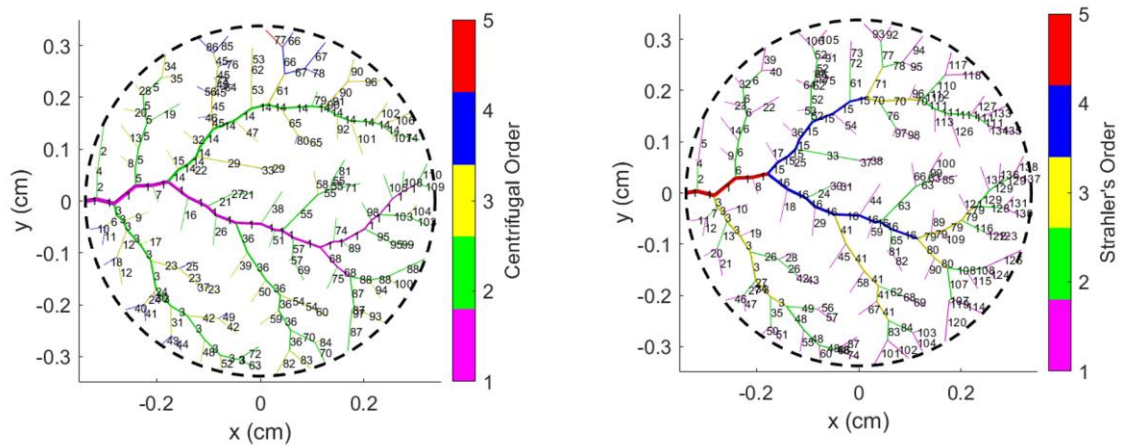


Figure 11. An example generated network with 100 bifurcations, with vessels colored by a) Strahler's order and b) Centrifugal order, where each segment is labelled a number which refers to the element that segments of the same number cumulatively compose.

To analyze the geometric properties of the generated networks, in Figures 12 and 13, all element values from ten randomly generated networks of size 900 bifurcations were accumulated, and the distributions of diameter and length for each order were plotted using Strahler's and centrifugal ordering respectively. The distribution of diameter can be approximated as Gaussian in both ordering schemes, though it shifts towards a more exponential distribution at the earlier orders for centrifugal ordering. The distribution of length is consistently more exponential for all orders and both ordering schemes. Alternatively, in Figure 14, elements from the same ten 900-bifurcation networks used in Figures 12 and 13 were compiled to calculate the mean diameter, mean length, and the number of the elements per centrifugal and Strahler's order. Due to the non-Gaussian distribution of geometric properties, the interquartile range is represented

by the error bars. Mean diameter and length decrease with increasing centrifugal order, while number of elements per centrifugal order demonstrates a Gaussian-like curve with increasing order. In Strahler's order, mean diameter and length increase with order, while number of elements decreases.

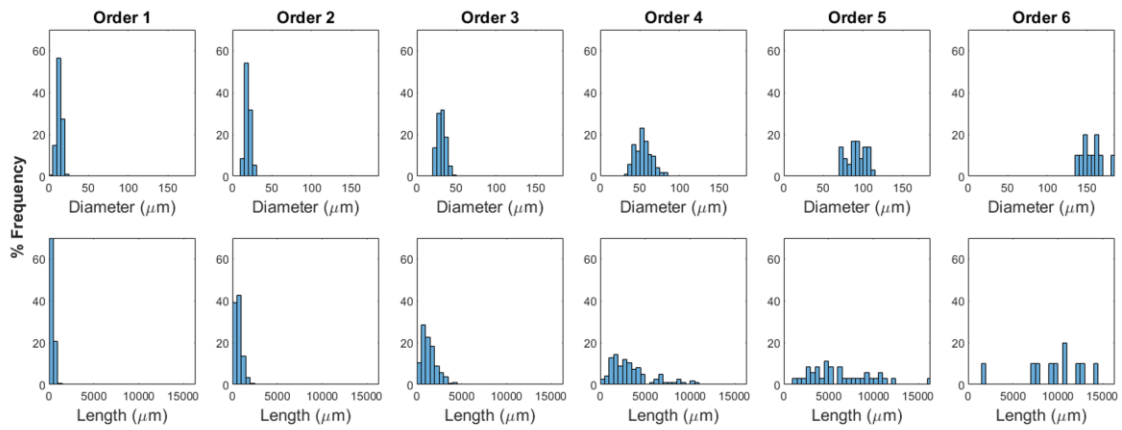


Figure 12. Frequency distributions of diameter (top row) and length (bottom row) in μm in Strahler's order, for elements accumulated from ten 900-bifurcation networks.

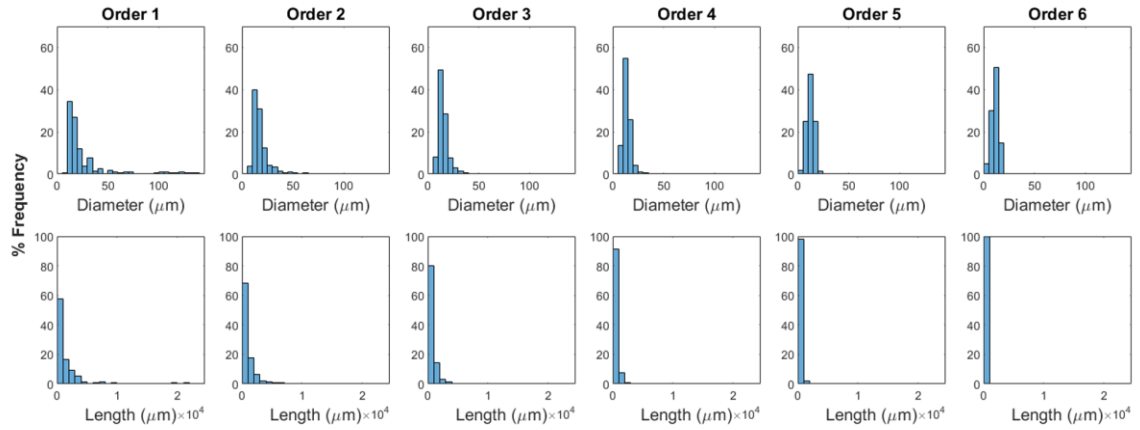


Figure 13. Frequency distributions of diameter (top row) and length (bottom row) in μm in centrifugal order, for elements accumulated from ten 900-bifurcation networks.

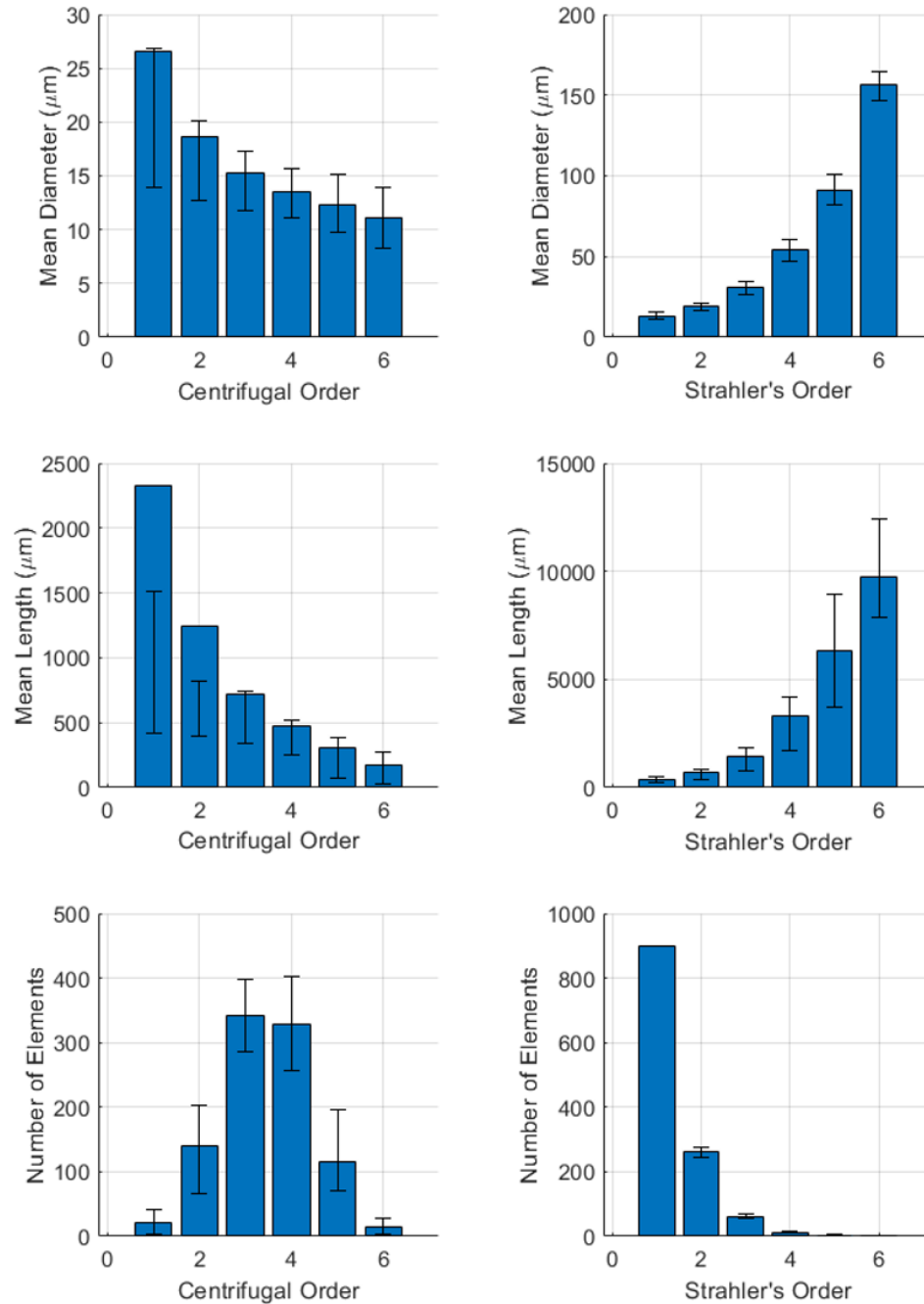


Figure 14. Mean diameter (μm), length (μm), and number of elements per centrifugal (left) and Strahler's (right) order, calculated over ten 900-bifurcation networks, where error bars represent interquartile range.

To compare and validate the geometric properties of the generated networks to that of previously published experimental data, in Figure 15, the model networks were grown to size 700 bifurcations with an *expVal* of 43%. Mean diameter, mean length, and number of elements per centrifugal order are compared between model results and previously collected microvascular data from rat gluteus maximus muscle (22), where the order of the diameter and length data has been decreased so that first-order diameters match between model and experiment. The model generally matches the experimental data well, suggesting successful validation, except for the first two orders of mean length per centrifugal order. There is also poor matching between model and experimental data for the number of elements per centrifugal order. To compare and validate the model's generated networks against another experimental dataset, in Figure 16, the model networks were grown to 300 bifurcations with an *expVal* of 54% and matched to vascular data in the rat spinotrapezius from Engelson et al. (38). For further fitting, model parameters *Aperf* and *Qperf* were adjusted from their default values to $3.6 \times 10^{-5} \text{ cm}^2$ and $1.2 \times 10^{-9} \text{ mL/s}$ respectively. The mean diameter, mean length, and number of elements per Strahler's order for the model fit well with the experimental data.

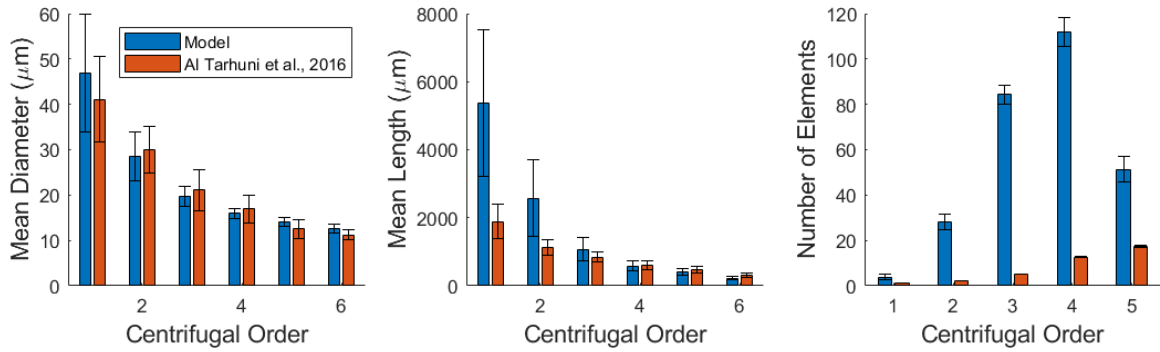


Figure 15. Mean diameter, mean length, and number of elements for each centrifugal order compared between model, for ten 700-bifurcation networks generated with $expVal = 43\%$, and rat gluteus maximus vasculature data from Al Tarhuni et al., 2016 (22). Data replotted from Figure 3 in (22), with permission and slight modification.

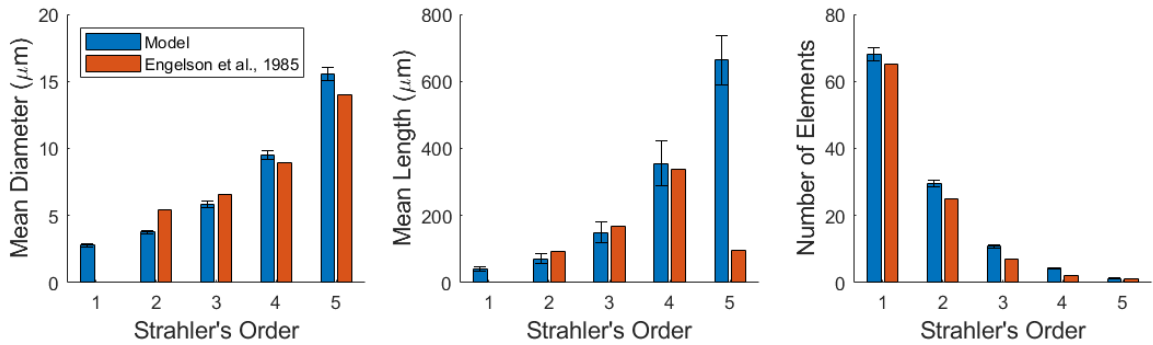


Figure 16. Mean diameter, mean length, and number of elements for each Strahler's order compared between model, for ten 300-bifurcation networks generated with $expVal = 54\%$, $Aperf = 3.6 \times 10^{-5} \text{ cm}^2$, $Qperf = 1.2 \times 10^{-9} \text{ mL/s}$, and rat spinotrapezius vasculature data from Engelson et al., 1985 (38).

For understanding of the generated networks' ability to demonstrate Horton's Law, in Figure 17, linear regression analysis was performed between each geometric

variable (diameter, length, and number of elements) and Strahler's or centrifugal order, calculated for ten model networks grown to 100 bifurcations – preliminary simulations demonstrated that for greater *Nbif* values (e.g., 900 bifurcations), results were similar. All calculated geometric variables presented had a strong linear fit ($R^2 > 0.9$), demonstrating Horton's Law, except for the number of elements per centrifugal order which demonstrates a poor linear fit ($R^2 = 0.236$). Strahler's order seems to yield a stronger linear fit than centrifugal order, based on the calculated coefficients of determination. Seeing that the model generally successfully demonstrates Horton's Law, Table 2 provides Horton's law ratio values calculated for both ordering schemes and using three different methods for ten 100-bifurcation networks. It can be observed that all three calculation methods yielded similar ratio values. While length ratio values seem similar between ordering schemes, with the diameter ratio being slightly less so, Strahler's order yields a significantly larger bifurcation ratio value compared to centrifugal order. For contextual understanding of the model's Horton's Law ratios against that of the literature, Table 3 demonstrates a literature review of Horton's law ratios published from other datasets, originally reviewed by Al Tarhuni (39). The table provides context regarding the model's Horton's ratios compared to that of other tissues found in literature. It can be observed that ratio values from the model, which is based on the rat gluteus maximus skeletal muscle microvasculature, are not only similar to ratio values of microvasculature from other skeletal muscle tissues, but also non-skeletal muscle microvasculature and bronchial trees.

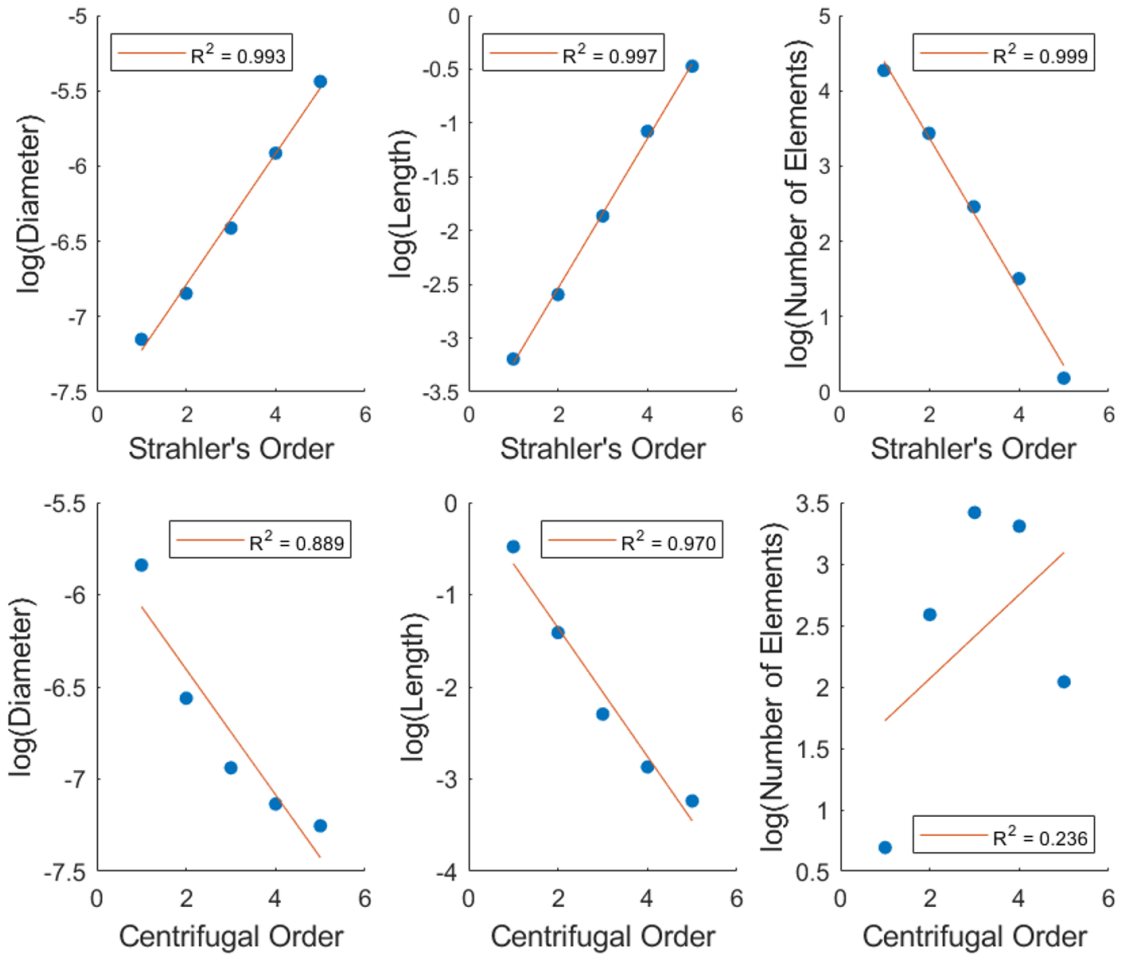


Figure 17. Linear regression analysis performed between each geometric variable (diameter, length, and number of elements) and Strahler's (top row) or centrifugal (bottom row) order, calculated for ten model networks grown to 100 bifurcations.

Table 2: The diameter (R_D), length (R_L), and bifurcation (R_B) ratios for centrifugal (left) and Strahler's (right) order, calculated using three different methods.

Method	Ratios (Centrifugal Strahler's)					
	Diameter (R_D)		Length (R_L)		Bifurcation (R_B)	
Regression for all networks combined	1.4167	1.6023	2.1311	2.0953	2.1629	4.0085
Average of regressions from each network	1.4763	1.6152	2.1560	2.1304	2.3153	4.1016
Regression of mean values from each network	1.4928	1.6167	2.1766	2.1568	2.1629	4.0085

Table 3: Horton’s Law ratios collected from literature for various types of tissues: skeletal muscle, non-skeletal muscle, and non-vascular tissue.

Tissue	RD	RL	RB	Reference
<i>Skeletal Muscle</i>				
Rat gluteus maximus	1.38	1.48	2.1	Al Tarhuni et al. 2016 (22)
Cat sartorius	1.25	1.86	3.17	Koller et al. 1987 (5)
Rat spinotrapezius	1.51	1.33	2.74	Engelson et al. 1985 (3)
Hamster cheek pouch retractor	1.63	2.59	3.43	Ellsworth et al. 1987 (3)
<i>Non-Skeletal Muscle</i>				
Human pulmonary arteries	1.59	1.49	2.99	Singhal et al. 1973 (42)
Human bulbar conjunctiva	1.26	1.36	2.77	Fenton & Zweifach 1985 (43)
Rabbit omentum	1.3	1.61	3.12	Fenton & Zweifach 1985 (43)
<i>Non-Vascular Tissue</i>				
Rat bronchial tree	1.53	1.82	3.31	Horsfield & Thurlbeck 1981 (44)
Human bronchial tree	1.43	1.4	2.81	Horsfield & Thurlbeck 1981 (44)

To explore the model’s user-adjustable parameters and their effect on the generated networks, Figure 18 explores changes in the Horton’s ratios \pm the 95% confidence interval based on single networks of 100 bifurcations generated under three different cases: case 1) varying Murray’s Law exponent γ , case 2) varying *Aperf*, and

case 3) varying Q_{perf} . Out of all tested properties, only the Murray's Law exponent appears to significantly affect the networks' Horton's ratios.

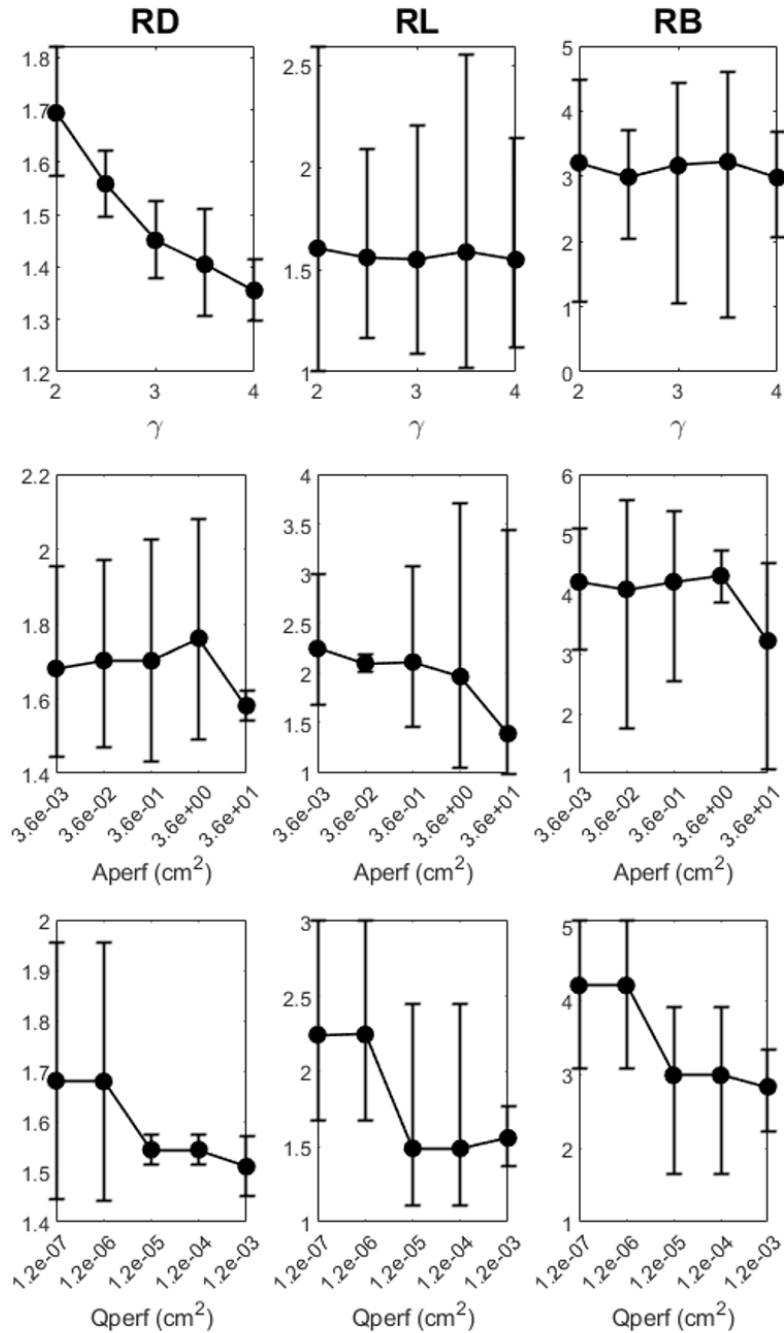


Figure 18. Five generated networks plotted as mean \pm 95% confidence interval, as the Horton's ratios are tested over three cases for $N_{bif} = 100$ bifurcations. Top row: varying Murray's law exponent γ . Middle row: varying the tissue size within which the network is generated A_{perf} . Bottom row: varying the amount of blood flowing through the terminal vessels of the network Q_{perf} .

To evaluate the generated networks' fractal dimension, in Table 4, the mean fractal dimension of three networks of size 100 bifurcations is calculated for varying numbers of boxes and averaged. As expected, the networks are fractal, and it does not appear that their fractal dimension changes significantly across varying levels of magnification for three randomized networks with the same model parameters. To evaluate the effect that the model's user-adjustable parameters have on fractal dimension, Figure 19 demonstrates changes in fractal dimension evaluated from networks of varying: number of bifurcations $Nbif$, terminal arteriole supply area $Aperf$, amounts of terminal arteriole blood flow $Qperf$, Murray's law exponents γ , and asymmetry limit $expVal$. Out of the listed properties, provided that all other parameters remain the same except for the property of interest, only $Nbif$ and $expVal$ affected the fractal dimension.

Table 4: Fractal dimension, calculated over varying levels of boxes using the box counting method, in which three individual networks are calculated and then averaged.

Number of boxes	Network 1	Network 2	Network 3	Averaged
1	1.5547	1.5597	1.5488	1.5544
100	1.5073	1.5130	1.5102	1.5102
300	1.5060	1.5119	1.5084	1.5088
500	1.5057	1.5116	1.5081	1.5085

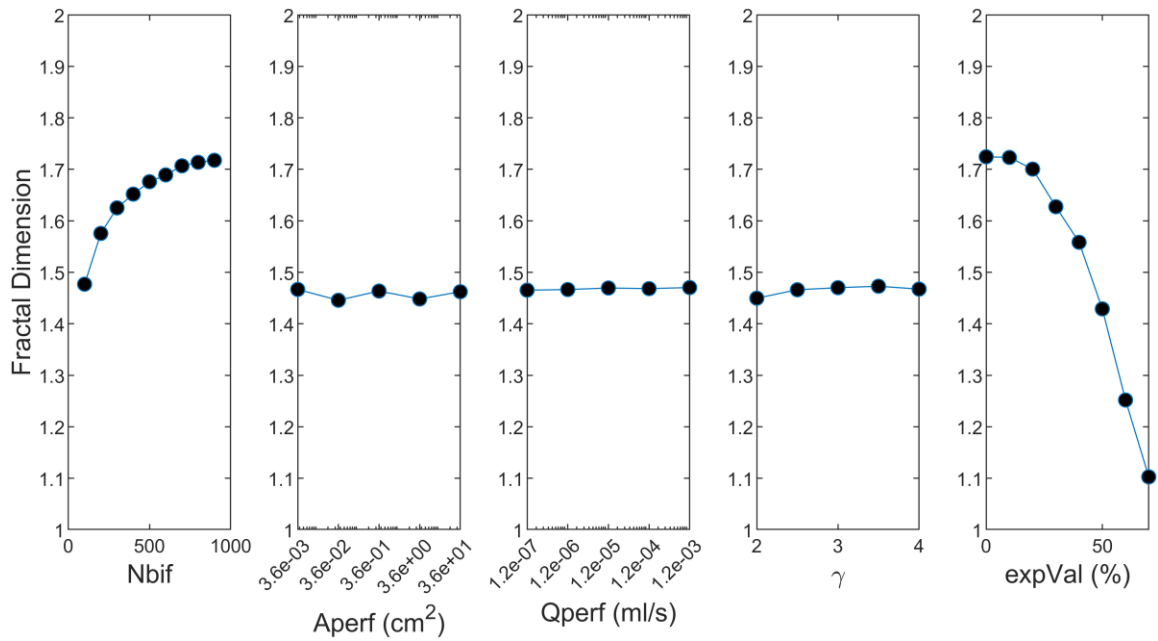


Figure 19. Fractal dimension calculated for single networks of 100 bifurcations over five varying model parameters: a) *Nbif*, b) *Aperf*, c) *Qperf*, d) γ , e) *expVal*. Aside from the varying model parameter, all other values were kept at default for these 100-bifurcation networks.

For understanding of the generated networks' ability to demonstrate Murray's law, in Figure 20, linear regression analysis was performed between the logarithmic transformations of flow and diameter of each segment of ten generated networks grown to 100. The calculated Murray's law exponent for this data is around 2.18. Murray's law exponent when excluding vessels with a diameter smaller than $20\mu\text{m}$ was 2.81.

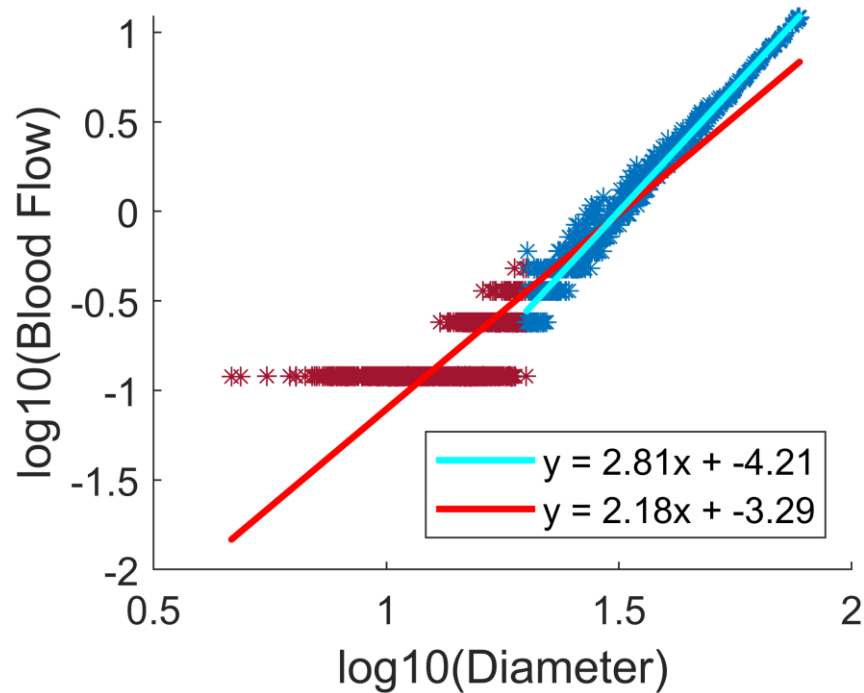


Figure 20. The logarithm of blood flow plotted vs. logarithm of diameter to evaluate the Murray's Law exponent. The starred points represent the logarithm of the blood flow-diameter value pairing for each segment within ten 100-bifurcations networks, while lines represent the linear fit applied. The red data represents the full model dataset, while the blue data represents excluding segments with diameters lower than $20 \mu\text{m}$, which attempts to approximate experimental conditions. Equations for the linear fits are presented in the legend.

For understanding of the generated networks' ability to demonstrate the network Fahraeus effect, in Figure 21, a cubic smoothing spline fit was plotted between the diameter and hematocrit of each segment accumulated from five networks of size 100 bifurcations which were generated with two-phase blood flow, based on maintaining constant blood flow at terminal vessels (case 2). The cubic smoothing spline fit is an interpolation of the data which may be used to estimate the trend when there is

substantial noise. Based on the cubic spline, the tube hematocrit appears to decrease with decreasing diameter, while discharge hematocrit increases slightly initially and then decreases as diameter approaches $10\mu\text{m}$. Both hematocrits stop decreasing around $10\mu\text{m}$, when tube hematocrit is around 0.25 and discharge hematocrit is around 0.38. The hematocrits increase significantly as diameter continues to decrease past $10\mu\text{m}$.

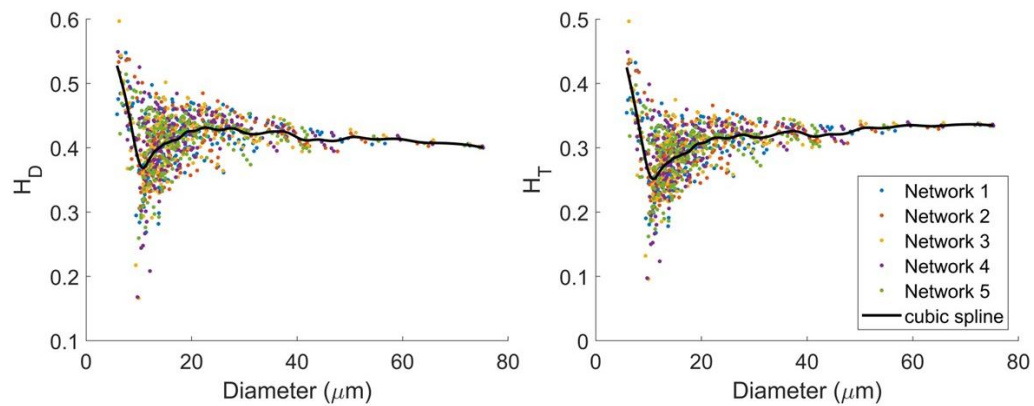


Figure 21. The discharge (left) and tube (right) hematocrit plotted versus diameter in μm for segments accumulated from five 100-bifurcation networks calculated with simulation case 2. Segment hematocrit-diameter values are colored based on the network they came from, and solid black lines represent the cubic spline fit.

2.4 Discussion

To summarize, a CCO-based network model was constructed to generate branching arteriolar networks in various skeletal muscles based on user-adjustable model parameters. The model was comprehensively validated according to previously collected rat gluteus

maximus vasculature data (22, 23), along with other skeletal muscle vasculature datasets which, though they may not be as comprehensive, support the model's capability of flexibly characterizing vascular data from different skeletal muscles and under different experimental conditions. Regarding which model properties affect the generated networks, the Murray's law exponent γ affects the networks' diameter ratio, and number of bifurcations $Nbif$ and $expVal$ affects the fractal dimension. While blood in the microvasculature may behave as a two-phase fluid of red blood cells and plasma, there was no significant effect between modelling blood as a single-phase fluid and two-phase fluid on the geometric properties of the generated networks. There was also no significant effect on the hemodynamic properties of the generated network when changing constant blood flow maintained at terminal vessels as is implemented in case 1 and case 2 to red blood cell flow, case 3.

Several factors may be considered which makes the present study unique in its presentation. Previous usage of CCO-based algorithms has commonly taken a more macrovascular view by focusing on arteries rather than arterioles; additionally, any usage of CCO on arterioles typically involved the generation of arterioles from pre-existing vasculature, rather than de novo. Additionally, the present work showcases in-depth the ability of CCO-generated networks to approximate the geometrical and topological features of real vasculature through validations to several relevant skeletal muscle experimental datasets. Validation of CCO-based models via comparison to experimental data has not been commonly performed in literature; while past work has demonstrated experimental validation of computational models following CCO-like algorithms (40), the experimental datasets have been limited in range of vessel diameters included, reflecting

previously discussed difficulties in acquiring data through experimental measures. The presented experimental validation of the model's *flow* properties, such as the Murray's Law exponent or the network Fahraeus effect, has not been commonly reported in relation to CCO, or computationally-generated vascular models in general, within the literature.

One notable finding in this study is the distinct difference between the two ordering schemes, centrifugal and Strahler's. The two ordering schemes have generally performed a similar role within the literature, and thus, have been assumed to be interchangeable. Recalling that order 1 refers to the terminal vessels in Strahler's order, and the inlet arteriole in centrifugal order, comparisons can be attempted between the two ordering schemes when one ordering scheme is flipped. Under ideal circumstances, the vessel properties per order should be comparable since the goal of ordering schemes is to identify vessels of similar properties as within the same 'class', or order. However, findings in the current study suggest that this is not the case.

In Figure 14, the variation in mean diameter, length, and number of bifurcation within each ordering scheme respectively is generated due to the randomization of sampled points included within the methods for network generation – this variation is expected and aligns with the goal to be able to generate different, but statistically similar networks, as is observable in real life where there may be slight individual-specific variations in growth when focusing on the exact same anatomies. The mean diameter, mean length, and number of elements per Strahler's order is approximately exponential, which aligns with previous findings (20, 33). Between ordering schemes, there is a large difference in data values, more than can be explained by the randomization of vessel placements inherent to the network generation algorithm; since the two ordering schemes

are used on the same ten networks, these differences in data values can only be attributed to the different ordering schemes. It can be assumed that differences in the categorization of segments into specific orders will result in differences in the grouping of segments into elements, which most of the presented geometric and hemodynamic statistics were calculated based on.

To further understand the significance of ordering schemes, Figure 11 provides a visual demonstration of how ordering scheme can result in greatly differing categorization of elements in a single network. Order 1 element identified according to centrifugal ordering starts from the inlet arteriole and extends all the way to a terminal vessel, while the order 5 (max order) element in Strahler's order gets cut off and splits into two order 4 elements, far before the terminal vessels. With the exact same network being used, differences in element numbering must result from the ordering scheme, as the two ordering schemes have different classifications of which segments compose an element.

Additionally, differences in ordering schemes can be further evaluated in Figure 12 and 13, which shows a difference in the distributions of elements per order for Strahler's and centrifugal ordering respectively. Model frequency distributions in Figure 13 demonstrate agreement with previously published centrifugally ordered experimental results in rat gluteus maximus vasculature (22) which suggest that diameter results have an approximately normal distribution ($R^2 > 0.8$ for most orders), while for length results, lesser centrifugal orders have a poorer fit ($R^2 = 0.2-0.4$) compared to larger centrifugal orders ($R^2 > 0.8$). The validation of Figure 13 reinforces the model's capability of generating networks with experimental distributions of geometric data. Additionally, if the generated networks in Figure 13 possess appropriate distributions of geometric data,

then the Strahler's distributions in Figure 12, which are based on the same networks, should be similarly appropriate. As such, the validation also reinforces the accuracy of these results which suggest a significant difference between the ordering schemes.

In summary, Figures 11, 12, 13 and 14 support the idea that the ordering scheme plays a significant role in what the expected network statistics will be per order and the two ordering schemes are not as comparable as one may think. Since the ordering scheme appears to play a significant role in the resulting statistics per order, it would be reasonable to suggest that for further validations to experimental data, the computational model should use the same ordering scheme as was experimentally used.

Regarding the model's performance in the validation with experimental data, with the adjustment of model parameters, the model compared well. In Figure 15, mean diameter matches between model and experimental measurements over all centrifugal orders. Mean length is not quite matched in orders 1 and 2, however this can be attributed to how the model and experimental data differ in the consideration of asymmetric bifurcations. In the model, *expVal* removes all vessels which are lower than a certain percentage of the parent. In the experimental data, however, there may be inconsistencies in terms of which asymmetric bifurcations are ignored or missed, and which are kept. Inconsistent inclusion and exclusion of small daughter vessels may result in more small daughters being included on large parent vessels, resulting in shorter elements being included in lower centrifugal orders, and hence, lower mean length in orders 1 and 2. Regarding the number of elements per order, the model data demonstrates a bell-like curve, which is expected of data collected based on a centrifugal ordering scheme (Figure 14). However, the experimental data seems almost exponential, with a significantly lower

number of elements per order, suggesting that there are many vessels that the experimental data may have missed. Generally, Figure 15 demonstrates that the model successfully simulates the experimental data, with discrepancies in length and number of elements per order being explainable by missed or ignored vessels in the experimental data.

As previously stated, to perform a stronger validation of the model, it was also compared to other skeletal muscle microvasculature datasets within the literature to overcome experimental limitations and inconsistencies between datasets. Engelson et al. (38) acquired vasculature data from the rat spinotrapezius muscle, and similarly published mean diameter, length, and number of elements per order, however, using the Strahler's ordering scheme. In Figure 16, when using Strahler's order, the model networks demonstrate good agreement with the experimental data for mean diameter, mean length, and number of elements per order. This is despite experimental limitations Engelson et al. describe in which there may be discrepancies in expected measured values due to unusually large branches which invariably connect transverse arterioles to capillary networks within the spinotrapezius muscle, resulting in higher order vessels being occasionally shorter than the length of the next lower order vessel. Overall, despite varying experimental limitations between the Al Tarhuni et al. and Engelson et al. datasets, the model was able to generate networks with comparable geometric properties to both datasets, supporting the model's flexibility in generating networks for various skeletal muscle vasculatures.

The following concerns the model's ability to demonstrate Horton's Law and comparisons of its Horton's Law ratios to the ratio values found in literature. In Figure

17, since the linear fits in all ratios and both ordering schemes are strong, it can be concluded that the model successfully demonstrates the experimentally proven Horton's Law. Strahler's order seems to yield a stronger fit compared to centrifugal order, which may be attributed to previously discussed differences in how elements are defined according to their ordering scheme. These findings suggest that Strahler's order yields a more exponential distribution of mean diameter, length, and number of elements per order (as plotted in Figure 14). The poor fit of the number of elements per centrifugal order can be related to the more Gaussian curve of the values in Figure 14.

Despite having found three different methods of calculating the Horton's Law ratios within literature, Table 2 demonstrates that all three methods yield similar ratio values. However, there is a notable difference in ratio values between the ordering schemes, especially concerning the bifurcation ratio. This difference can once again be attributed to differences in segment ordering and element categorization between the ordering schemes. As is reflected in Figure 11, out of all geometric properties, the number of elements per order is most differently described by the two ordering schemes.

When comparing the model's centrifugal ordering scheme ratios in Table 2 to that of the experimental data from Al Tarhuni et al. 2016 (Table 3), the ratio values are similar. The difference in RL can be attributed to experimental inconsistencies with missing vessels at asymmetric bifurcations. While Strahler's order yields ratios which are further from expected experimental values, by using *expVal* set to 60%, the Strahler's order ratios become RD, RL, and RB = 1.5, 2.1, and 2.7, respectively, for all three methods for centrifugal ordering ($R^2 > 0.9$), which is closer to skeletal muscle vasculature datasets such as Koller et. al., 1987 (5), Engelson et al., 1985 (38) and Ellsworth et al.,

1987 (3), which used Strahler ordering to calculate their ratios. The agreement of the model's ratios and the ratios in Table 3 demonstrates that with adjustments, the model can agree with ratios from other datasets, including even non-skeletal muscle vasculature and non-vascular tissue. The agreement of values regardless of physiology suggests that there is an optimization of geometric properties in biological branching network structures which the model is capable of capturing.

Fractal analysis results can be found in Table 4, where the fractal dimension for networks generated with default model parameters were calculated to be consistently around 1.5. The mean \pm SD of the fractal dimension of eight arteriolar networks in the rat gluteus maximus muscle has previously been found to be 1.3844 ± 0.02 (22). Figure 19 demonstrates that by adjusting the number of bifurcations *Nbif* and *expVal* of the generated networks, the fractal dimension of the resulting networks can be adjusted. For example, to achieve a fractal dimension of around 1.3844 from the experimental data, model parameters can be adjusted to *expVal* = 40-50%.

Figure 20 presents the first of the current study's hemodynamic results, showing the model's ability to demonstrate Murray's law when user-adjusted parameters are changed from default to experimental conditions. The concept of element as defined by centrifugal or Strahler's order was not used for this analysis, as Murray's law relates purely to the blood flow within and diameter of vessels, without concern for vessel length. Thus, no artifacts should have been introduced by differing element categorization. While the calculated Murray's law exponent was around 2.18, the exponent when excluding smaller vessels (with diameters lower than 20 μ m) is 2.81, which is closer to the value of 2.63 measured in the rat gluteus maximus arteriolar

vasculature (23). The exclusion of smaller vessels was performed to simulate experimental conditions, in which smaller vessels may be missed during the data collection process. A possible explanation of why the calculated Murray's Law exponent from the ten generated networks does not align with the model's input Murray's Law exponent value γ , which was set to 2.6, is that γ was used to characterize the diameter-flow relationship at individual bifurcations during network generation and does not extend to characterizing the relationship between diameter and flow for segments accumulated from the entire network.

Regarding the impact of adjusting model parameters on the resulting generated networks, Figure 18 demonstrates that the only parameter that significantly affects the Horton's ratios of the generated networks is the Murray's Law exponent γ , which is expected, as γ characterizes the power law relationship between diameter and blood flow. Since the relationship between diameter and blood flow is otherwise maintained by γ , increases to Q_{perf} result in proportional increases in diameter and blood flow such that the ratios are not significantly affected. Similarly, increases to A_{perf} and N_{bif} only caused proportional increases in diameter, length, and number of elements. Though Q_{perf} and A_{perf} do not significantly affect the geometric features of the generated networks, they may still be adjusted, given the experimental data, to affect hemodynamic properties such as O_2 delivery.

Finally, Figure 21 presents the model's ability to demonstrate the Fahraeus and network Fahraeus effects. In Figure 21, the cubic spline-based decreases in tube and discharge hematocrit as diameter approaches $10\mu\text{m}$ align with experimental findings (41)

in demonstrating the network Fahraeus effect. The increases in both discharge and tube hematocrit around the 10 μ m diameter mark correspond with the reverse Fahraeus and reverse network Fahraeus effects, proving that the model successfully incorporates both hemodynamic properties.

The utility of the presented network model is far-reaching for any investigations related to the skeletal muscle microvasculature, as its adjustable parameters provide a convenient way of allowing experimenters to confirm results and test/refine novel hypotheses across branching arteriolar networks within various skeletal muscle tissues. While anatomical variability has been explored before with CCO-based algorithms, models for arteriolar branching networks within skeletal muscle tissue is a niche that has not been commonly addressed, as most CCO-based models continue to focus on more macrovascular vessel structures.

A few limitations in the present work are as follows: Firstly, the computation time of the model is long compared to other existing models (31). At its current state, it takes around 12 hours for the average CPU to generate a 900-bifurcation network. Further optimizations towards reducing computation time are expected to be implemented in future work. Inconsistencies in and between experimental datasets make it hard to perfectly validate the model, as with the parameter adjustments considered, the model struggles to exactly match any specific experimental dataset. Additionally, data from the literature tended to be limited in comparison to the rat gluteus maximus experimental data, and hence may not have captured muscle-specific properties for the model to simulate; for example, arteriolar networks in highly oxidative muscles may contain properties which are not present in glycolytic and fast-twitch muscles such as the gluteus

maximus. Nevertheless, the model has been proven to be adaptable enough to approximate experimental data of vasculature in various skeletal muscles, and thus the model may be viewed as representing an ‘average’ of what the skeletal muscle vasculatures generally resemble on a statistical basis.

Being that the overarching goal is to develop a CCO-based model which will generate networks for any tissue, the scope of the present model will be greatly expanded in future work, and a version of the model that is more readily usable for a broader readership will be made available to others. While the current model can only characterize branching arteriolar networks, future work will aim to increase the complexity of the vasculature geometry to incorporate arcading structures into the vessel network. To enable simulation of vasculature within a broader option of physiologies, the model’s perfused tissue space will be expanded from a 2D circular area to incorporate customizable tissue areas for non-uniform and 3D tissue geometries. These changes to allow for more customization of the vasculature should allow for closer matching to experimental data, and should enable completion of experimental microvascular datasets. It should also enable computational modeling of blood-tissue oxygen transport based on complete 3D arteriolar networks. Most importantly, the model will be expanded to incorporate regulators of arteriolar diameter (e.g., vasodilators, oxygen, etc.), such that the generated networks can respond to stimuli by changing vessel diameter, and thus tissue perfusion, in real time. Such developments will allow the model to make great strides towards simulating adaptive or maladaptive situations at the site of vasculature-tissue blood flow exchange, which would be highly beneficial for understanding how

vascular mechanisms come together in a myriad of multi-scale interactions to regulate the blood circulatory system in a way that results in healthy vs. disease outcomes.

2.5 Summary

The present work introduces a CCO-based algorithm for simulating branching arteriolar networks in healthy skeletal muscle tissue that is relatively thin. Comprehensive comparison of the network hemodynamic and geometric properties to experimental data collected both previously at our institution and from other literature demonstrates the model's flexibility in potentially approximating microvasculature in various skeletal muscles, given that some model parameters (e.g., γ and $Nbif$) were not adjusted for specific muscles considered. Understanding of arteriolar behavior within the microvasculature is conducive to understanding complex health conditions due to its role in flow regulation and proximity to the capillary bed, the site of blood flow exchange between tissue and circulatory system, and this model can act as an alternative solution to challenges inherent in experimental procedures. This model is one of few comprehensively validated CCO-based models to focus on the simulation of microvasculature within any skeletal muscle via the adjustment of model parameters, making it a beneficial and widely applicable investigative tool to perform hypothesis testing and validation for microvasculature in various skeletal muscle tissues.

2.6 References

1. **Secomb TW.** Theoretical Models for Regulation of Blood Flow. *Microcirculation* 15: 765–775, 2008. doi: 10.1080/10739680802350112.
2. **Pries AR, Secomb TW, Gessner T, Sperandio MB, Gross JF, Gaehtgens P.** Resistance to blood flow in microvessels in vivo. *Circ Res* 75: 904–915, 1994. doi: 10.1161/01.RES.75.5.904.
3. **Ellsworth ML, Liu A, Dawant B, Popel AS, Pittman RN.** Analysis of vascular pattern and dimensions in arteriolar networks of the retractor muscle in young hamsters. *Microvascular Research* 34: 168–183, 1987. doi: 10.1016/0026-2862(87)90051-3.
4. **Pries AR, Secomb TW, Gaehtgens P.** Relationship between structural and hemodynamic heterogeneity in microvascular networks. *American Journal of Physiology-Heart and Circulatory Physiology* 270: H545–H553, 1996. doi: 10.1152/ajpheart.1996.270.2.H545.
5. **Koller A, Dawant B, Liu A, Popel AS, Johnson PC.** Quantitative analysis of arteriolar network architecture in cat sartorius muscle. *American Journal of Physiology-Heart and Circulatory Physiology* 253: H154–H164, 1987. doi: 10.1152/ajpheart.1987.253.1.H154.
6. **Lapi D, Di Maro M, Mastantuono T, Starita N, Ursino M, Colantuoni A.** Arterial Network Geometric Characteristics and Regulation of Capillary Blood Flow in Hamster Skeletal Muscle Microcirculation. *Front Physiol* 9: 1953, 2019. doi: 10.3389/fphys.2018.01953.
7. **Frisbee JC, Wu F, Goodwill AG, Butcher JT, Beard DA.** Spatial heterogeneity in skeletal muscle microvascular blood flow distribution is increased in the metabolic syndrome. *American Journal of Physiology-Regulatory, Integrative and Comparative Physiology* 301: R975–R986, 2011. doi: 10.1152/ajpregu.00275.2011.
8. **Fleming BP, Barron KW, Howes TW, Smith JK.** Response of the microcirculation in rat cremaster muscle to peripheral and central sympathetic stimulation. *Circ Res* 61: II26-31, 1987.
9. **Ii S, Kitade H, Ishida S, Imai Y, Watanabe Y, Wada S.** Multiscale modeling of human cerebrovasculature: A hybrid approach using image-based geometry and a mathematical algorithm. *PLoS Comput Biol* 16: e1007943, 2020. doi: 10.1371/journal.pcbi.1007943.
10. **Jaquet C, Najman L, Talbot H, Grady L, Schaap M, Spain B, Kim HJ, Vignon-Clementel I, Taylor CA.** Generation of Patient-Specific Cardiac Vascular Networks: A Hybrid Image-Based and Synthetic Geometric Model. *IEEE Trans Biomed Eng* 66: 946–955, 2019. doi: 10.1109/TBME.2018.2865667.

11. **Papamanolis L, Kim HJ, Jaquet C, Sinclair M, Schaap M, Danad I, van Diemen P, Knaapen P, Najman L, Talbot H, Taylor CA, Vignon-Clementel I.** Myocardial Perfusion Simulation for Coronary Artery Disease: A Coupled Patient-Specific Multiscale Model. *Ann Biomed Eng* 49: 1432–1447, 2021. doi: 10.1007/s10439-020-02681-z.
12. **Gross J, Intaglietta M, Zweifach B.** Network model of pulsatile hemodynamics in the microcirculation of the rabbit omentum. *American Journal of Physiology-Legacy Content* 226: 1117–1123, 1974. doi: 10.1152/ajplegacy.1974.226.5.1117.
13. **Gottlieb ME.** Modelling Blood Vessels: A Deterministic Method With Fractal Structure Based On Physiological Rules. In: [1990] *Proceedings of the Twelfth Annual International Conference of the IEEE Engineering in Medicine and Biology Society*. [1990] Twelfth Annual International Conference of the IEEE Engineering in Medicine and Biology Society. IEEE, p. 1386–1387.
14. **Nekka F, Kyriacos S, Kerrigan C, Cartilier L.** A model of growing vascular structures. *Bltm Mathcal Biology* 58: 409–424, 1996. doi: 10.1007/BF02460590.
15. **Schreiner W.** Computer generation of complex arterial tree models. *Journal of Biomedical Engineering* 15: 148–150, 1993. doi: 10.1016/0141-5425(93)90046-2.
16. **Smith NP, Pullan AJ, Hunter PJ.** Generation of an Anatomically Based Geometric Coronary Model. *Annals of Biomedical Engineering* 28: 14–25, 2000. doi: 10.1114/1.250.
17. **Zamir M.** On Fractal Properties of Arterial Trees. *Journal of Theoretical Biology* 197: 517–526, 1999. doi: 10.1006/jtbi.1998.0892.
18. **Di Ieva A, Grizzi F, Ceva-Grimaldi G, Russo C, Gaetani P, Aimar E, Levi D, Pisano P, Tancioni F, Nicola G, Tschabitscher M, Dioguardi N, Baena RRY.** Fractal dimension as a quantitor of the microvasculature of normal and adenomatous pituitary tissue. *J Anatomy* 211: 673–680, 2007. doi: 10.1111/j.1469-7580.2007.00804.x.
19. **Schreiner W, Neumann F, Neumann M, End A, Roedler SM, Aharinejad S.** The influence of optimization target selection on the structure of arterial tree models generated by constrained constructive optimization. *Journal of General Physiology* 106: 583–599, 1995. doi: 10.1085/jgp.106.4.583.
20. **Schreiner W, Neumann F, Neumann M, End A, Roedler SM.** Anatomical Variability and Functional Ability of Vascular Trees Modeled by Constrained Constructive Optimization. *Journal of Theoretical Biology* 187: 147–158, 1997. doi: 10.1006/jtbi.1997.0413.
21. **Schreiner W, Neumann F, Karch R, Neumann M, Roedler SM, End A.** Shear Stress Distribution in Arterial Tree Models, Generated by Constrained Constructive

- Optimization. *Journal of Theoretical Biology* 198: 27–45, 1999. doi: 10.1006/jtbi.1999.0898.
22. **Al Tarhuni M, Goldman D, Jackson DN.** Comprehensive *In Situ* Analysis of Arteriolar Network Geometry and Topology in Rat Gluteus Maximus Muscle. *Microcirculation* 23: 456–467, 2016. doi: 10.1111/micc.12292.
 23. **Al-Khazraji BK, Novielli NM, Goldman D, Medeiros PJ, Jackson DN.** A Simple “Streak Length Method” for Quantifying and Characterizing Red Blood Cell Velocity Profiles and Blood Flow in Rat Skeletal Muscle Arterioles: Red Blood Cell Velocity Profiles in Arterioles. *Microcirculation* 19: 327–335, 2012. doi: 10.1111/j.1549-8719.2012.00165.x.
 24. **Schneider CA, Rasband WS, Eliceiri KW.** NIH Image to ImageJ: 25 years of image analysis. *Nat Methods* 9: 671–675, 2012. doi: 10.1038/nmeth.2089.
 25. **Karperien A.** FracLac for ImageJ; JavaDoc, source code, and jar,(Version 2.5)[Software]. *Albury, NSW: Charles Sturt University Retrieved October 1: 2011, 2001.*
 26. **Pries AR, Schonfeld D, Gaehtgens P, Kiani MF, Cokelet GR.** Diameter variability and microvascular flow resistance. *American Journal of Physiology-Heart and Circulatory Physiology* 272: H2716–H2725, 1997. doi: 10.1152/ajpheart.1997.272.6.H2716.
 27. **Pries AR, Secomb TW, Gaehtgens P, Gross JF.** Blood flow in microvascular networks. Experiments and simulation. *Circ Res* 67: 826–834, 1990. doi: 10.1161/01.RES.67.4.826.
 28. **Al-Khazraji BK, Saleem A, Goldman D, Jackson DN.** From one generation to the next: a comprehensive account of sympathetic receptor control in branching arteriolar trees: Regional differences in SNS receptor activation. *J Physiol* 593: 3093–3108, 2015. doi: 10.1113/JP270490.
 29. **Goldman D, Popel AS.** A Computational Study of the Effect of Capillary Network Anastomoses and Tortuosity on Oxygen Transport. *Journal of Theoretical Biology* 206: 181–194, 2000. doi: 10.1006/jtbi.2000.2113.
 30. **Pries AR, Neuhaus D, Gaehtgens P.** Blood viscosity in tube flow: dependence on diameter and hematocrit. *American Journal of Physiology-Heart and Circulatory Physiology* 263: H1770–H1778, 1992. doi: 10.1152/ajpheart.1992.263.6.H1770.
 31. **Schreiner W, Buxbaum PF.** Computer-optimization of vascular trees. *IEEE Trans Biomed Eng* 40: 482–491, 1993. doi: 10.1109/10.243413.
 32. **Lapi D, Marchiafava PL, Colantuoni A.** Geometric Characteristics of Arterial Network of Rat Pial Microcirculation. *J Vasc Res* 45: 69–77, 2008. doi: 10.1159/000109078.

33. **VanBavel E, Spaan JA.** Branching patterns in the porcine coronary arterial tree. Estimation of flow heterogeneity. *Circ Res* 71: 1200–1212, 1992. doi: 10.1161/01.RES.71.5.1200.
34. **Woldenberg MJ.** Quantitative Analysis of Biological and Fluvial Networks. In: *Microvascular Networks: Experimental and Theoretical Studies*. S. Karger AG, 1986, p. 12–26.
35. **Murray CD.** The Physiological Principle of Minimum Work: I. The Vascular System and the Cost of Blood Volume. *Proc Natl Acad Sci USA* 12: 207–214, 1926. doi: 10.1073/pnas.12.3.207.
36. **Kassab GS.** Scaling laws of vascular trees: of form and function. *American Journal of Physiology-Heart and Circulatory Physiology* 290: H894–H903, 2006. doi: 10.1152/ajpheart.00579.2005.
37. **Pries AR, Secomb TW, Gaetgens P.** Biophysical aspects of blood flow in the microvasculature. *Cardiovascular Research* 32: 654–667, 1996. doi: 10.1016/S0008-6363(96)00065-X.
38. **Engelson ET, Skalak TC, Schmid-Schönbein GW.** The microvasculature in skeletal muscle. *Microvascular Research* 30: 29–44, 1985. doi: 10.1016/0026-2862(85)90035-4.
39. **Al Tarhuni M.** Comprehensive Topological, Geometric, And Hemodynamic Analysis Of The Rat Gluteus Maximus Arteriolar Networks [Online]. <https://api.semanticscholar.org/CorpusID:13821825>.
40. **Lee T, Hong J, Yoo SS, Kim DW.** A computational modeling of blood flow in asymmetrically bifurcating microvessels and its experimental validation. *Numer Methods Biomed Eng* 34: e2981, 2018. doi: 10.1002/cnm.2981.
41. **House SD, Lipowsky HH.** Microvascular hematocrit and red cell flux in rat cremaster muscle. *American Journal of Physiology-Heart and Circulatory Physiology* 252: H211–H222, 1987. doi: 10.1152/ajpheart.1987.252.1.H211.

Chapter 3

3 Conclusion

3.1 Thesis Contributions

This thesis attempts to answer a central question involved in developing computational models for microvascular networks: how should you specify network's geometry and topology? The literature has introduced many methods for approximating network architecture, these methods often do not incorporate the structural and hemodynamic heterogeneity of real-life vasculature (1, 2). Since vascular function has been tied to network heterogeneity (2, 3), computational models aiming to simulate real life vasculature should incorporate the irregularity of microvascular geometry and topology.

The computational model presented within this thesis attempts to replicate real life skeletal muscle microvascular architecture using a CCO-based algorithm. CCO was chosen due to its ability to generate visually and statistically realistic vascular trees in the literature (4, 5). While CCO has commonly been applied to macrovasculature, it is seldom employed to model microcirculation, making the presented model a unique exploration of CCO application. To verify the model's closeness to real life, we validated the generated networks via comparison with experimental datasets collected in skeletal muscle over a comprehensive list of geometric and hemodynamic statistics. While most models are tissue-specific, this model introduces user-adjustable parameters which may be altered to better fit different data sets, contributing as an example towards future work

in developing adaptable network models. Another notable contribution of this thesis is the analysis of the commonly used ordering schemes, Strahler's and centripetal, for microvascular networks. The common purpose of ordering schemes is to group vessels with common properties, yet it was demonstrated in this thesis that the Strahler's and centripetal ordering schemes yield significantly different representations of identical networks.

3.2 Future Directions

As mentioned within Chapter 2, future work will aim to expand the capabilities of the presented model. Relevant tasks are as follows: the model may include adjustable parameters to fit the tissue perfusion area to specific tissues/organs. The model may also have adjustable hemodynamic and perfusion resistance parameters to enable simulation of health vs. disease conditions and experimental challenges; the outcome will be highly applicable to any demographic-specific modifications (e.g., sex, age, etc.). Future work will also implement the ability to simulate oxygen transport via blood.

Of all relevant tasks, we have given priority to the simulation of arteriolar behavior in response to the integration of various regulation mechanisms. While vascular models have been created, the incorporation of vasoregulatory mechanisms across a vessel network tree has not been widely explored. Models present in the literature thus far are often static geometric structures with unchanging diameters, ignoring vasomotion. Models which do without consideration of vessel behavior are often limited in resolution, focusing on the animation of a single vessel.

In previous work from Halvorson et al. 2023 (6), arteriolar response to the simulation of five well known vasoregulators was measured: metabolism (via adenosine concentration), adrenergic activation (via norepinephrine concentration), myogenic activation (altered intravascular pressure), oxygen (superfusate PO_2), and wall shear rate (altered intraluminal flow). This work, which was conducted within arterioles of healthy Zucker rat skeletal muscle tissue, aimed to establish a systematic approach for understanding the integrated regulation of skeletal muscle arteriolar tone. The result is a comprehensive experimental dataset of changes in arteriolar diameter against five chosen vasoregulators, in combinations from one up to three. Additionally, two machine learning models were trained on the experimental data to integrate the five regulation mechanisms and provide an arteriolar diameter prediction. Both machine learning models performed well, demonstrating high accuracy when compared to experimental data ($R^2 > 0.9$).

In the future, we aim to incorporate the machine learning models with our CCO-based network generation model, both of which were created and validated based on experimental arteriolar data within healthy rat skeletal muscle. After our CCO-based model (which has been validated in Chapter 2) generates an arteriolar network, the machine learning models should be able to adjust vessel diameters as appropriate when provided with data for the five regulation mechanisms. As a result, the combined models will yield arteriolar networks based on the principle of optimization (CCO) which are sensitive to moment-by-moment vasoregulation. The incorporation of vasoregulation into our CCO-based model will hold significance in the investigation of arteriolar network behavior in varying physiological states (e.g., disease and exercise) or in varying moments of time (e.g. over the cardiac cycle). If vasoregulation data is provided at high

time resolutions, then second-by-second animation of arteriolar network behavior may be possible.

3.3 References

1. **Pries AR, Secomb TW, Gaehtgens P, Gross JF.** Blood flow in microvascular networks. Experiments and simulation. *Circ Res* 67: 826–834, 1990. doi: 10.1161/01.RES.67.4.826.
2. **Pries AR, Secomb TW, Gaehtgens P.** Structure and hemodynamics of microvascular networks: heterogeneity and correlations. *American Journal of Physiology-Heart and Circulatory Physiology* 269: H1713–H1722, 1995. doi: 10.1152/ajpheart.1995.269.5.H1713.
3. **Pries AR, Secomb TW, Gaehtgens P.** Relationship between structural and hemodynamic heterogeneity in microvascular networks. *American Journal of Physiology-Heart and Circulatory Physiology* 270: H545–H553, 1996. doi: 10.1152/ajpheart.1996.270.2.H545.
4. **Schreiner W, Neumann M, Neumann F, Roedler SM, End A, Buxbaum P, Müller MR, Spieckermann P.** The branching angles in computer-generated optimized models of arterial trees. *Journal of General Physiology* 103: 975–989, 1994. doi: 10.1085/jgp.103.6.975.
5. **Karch R, Neumann F, Neumann M, Schreiner W.** A three-dimensional model for arterial tree representation, generated by constrained constructive optimization. *Computers in Biology and Medicine* 29: 19–38, 1999. doi: 10.1016/S0010-4825(98)00045-6.
6. **Halvorson BD, Bao Y, Ward AD, Goldman D, Frisbee JC.** Regulation of Skeletal Muscle Resistance Arteriolar Tone: Integration of Multiple Mechanisms.

Appendix – Figure Permissions

JOHN WILEY AND SONS LICENSE TERMS AND CONDITIONS

Mar 01, 2024

This Agreement between Daniel Goldman ("You") and John Wiley and Sons ("John Wiley and Sons") consists of your license details and the terms and conditions provided by John Wiley and Sons and Copyright Clearance Center.

License Number	5740250605881
License date	Mar 01, 2024
Licensed Content Publisher	John Wiley and Sons
Licensed Content Publication	Microcirculation
Licensed Content Title	Comprehensive In Situ Analysis of Arteriolar Network Geometry and Topology in Rat Gluteus Maximus Muscle
Licensed Content Author	Dwayne N. Jackson, Daniel Goldman, Mohammed Al Tarhuni
Licensed Content Date	Aug 12, 2016
Licensed Content Volume	23
Licensed Content Issue	6
Licensed Content Pages	12
Type of use	Journal/Magazine

Requestor type	Author of this Wiley article
Is the reuse sponsored by or associated with a pharmaceutical or medical products company?	no
Format	Print and electronic
Portion	Figure/table
Number of figures/tables	1
Will you be translating?	No
Circulation	5000 - 9999
Title of new article	A CONSTRAINED CONSTRUCTIVE OPTIMIZATION MODEL OF BRANCHING ARTERIOLAR NETWORKS IN RAT SKELETAL MUSCLE
Lead author	Yuki Bao
Title of targeted journal	Journal of Applied Physiology
Publisher	American Physiological Society
Expected publication date	Mar 2024
Portions	Figure 3: top, middle, bottom
Requestor Location	Daniel Goldman 

Attn: Daniel Goldman

Publisher Tax ID EU826007151

Total 0.00 USD

Terms and Conditions

TERMS AND CONDITIONS

This copyrighted material is owned by or exclusively licensed to John Wiley & Sons, Inc. or one of its group companies (each a "Wiley Company") or handled on behalf of a society with which a Wiley Company has exclusive publishing rights in relation to a particular work (collectively "WILEY"). By clicking "accept" in connection with completing this licensing transaction, you agree that the following terms and conditions apply to this transaction (along with the billing and payment terms and conditions established by the Copyright Clearance Center Inc., ("CCC's Billing and Payment terms and conditions"), at the time that you opened your RightsLink account (these are available at any time at <http://myaccount.copyright.com>).

Terms and Conditions

- The materials you have requested permission to reproduce or reuse (the "Wiley Materials") are protected by copyright.
- You are hereby granted a personal, non-exclusive, non-sub licensable (on a stand-alone basis), non-transferable, worldwide, limited license to reproduce the Wiley Materials for the purpose specified in the licensing process. This license, **and any CONTENT (PDF or image file) purchased as part of your order**, is for a one-time use only and limited to any maximum distribution number specified in the license. The first instance of republication or reuse granted by this license must be completed within two years of the date of the grant of this license (although copies prepared before the end date may be distributed thereafter). The Wiley Materials shall not be used in any other manner or for any other purpose, beyond what is granted in the license. Permission is granted subject to an appropriate acknowledgement given to the author, title of the material/book/journal and the publisher. You shall also duplicate the copyright notice that appears in the Wiley publication in your use of the Wiley Material. Permission is also granted on the understanding that nowhere in the text is a previously published source acknowledged for all or part of this Wiley Material. Any third party content is expressly excluded from this permission.
- With respect to the Wiley Materials, all rights are reserved. Except as expressly granted by the terms of the license, no part of the Wiley Materials may be copied, modified, adapted (except for minor reformatting required by the new Publication), translated, reproduced, transferred or distributed, in any form or by any means, and

no derivative works may be made based on the Wiley Materials without the prior permission of the respective copyright owner. **For STM Signatory Publishers clearing permission under the terms of the [STM Permissions Guidelines](#) only, the terms of the license are extended to include subsequent editions and for editions in other languages, provided such editions are for the work as a whole in situ and does not involve the separate exploitation of the permitted figures or extracts,** You may not alter, remove or suppress in any manner any copyright, trademark or other notices displayed by the Wiley Materials. You may not license, rent, sell, loan, lease, pledge, offer as security, transfer or assign the Wiley Materials on a stand-alone basis, or any of the rights granted to you hereunder to any other person.

- The Wiley Materials and all of the intellectual property rights therein shall at all times remain the exclusive property of John Wiley & Sons Inc, the Wiley Companies, or their respective licensors, and your interest therein is only that of having possession of and the right to reproduce the Wiley Materials pursuant to Section 2 herein during the continuance of this Agreement. You agree that you own no right, title or interest in or to the Wiley Materials or any of the intellectual property rights therein. You shall have no rights hereunder other than the license as provided for above in Section 2. No right, license or interest to any trademark, trade name, service mark or other branding ("Marks") of WILEY or its licensors is granted hereunder, and you agree that you shall not assert any such right, license or interest with respect thereto
- NEITHER WILEY NOR ITS LICENSORS MAKES ANY WARRANTY OR REPRESENTATION OF ANY KIND TO YOU OR ANY THIRD PARTY, EXPRESS, IMPLIED OR STATUTORY, WITH RESPECT TO THE MATERIALS OR THE ACCURACY OF ANY INFORMATION CONTAINED IN THE MATERIALS, INCLUDING, WITHOUT LIMITATION, ANY IMPLIED WARRANTY OF MERCHANTABILITY, ACCURACY, SATISFACTORY QUALITY, FITNESS FOR A PARTICULAR PURPOSE, USABILITY, INTEGRATION OR NON-INFRINGEMENT AND ALL SUCH WARRANTIES ARE HEREBY EXCLUDED BY WILEY AND ITS LICENSORS AND WAIVED BY YOU.
- WILEY shall have the right to terminate this Agreement immediately upon breach of this Agreement by you.
- You shall indemnify, defend and hold harmless WILEY, its Licensors and their respective directors, officers, agents and employees, from and against any actual or threatened claims, demands, causes of action or proceedings arising from any breach of this Agreement by you.
- IN NO EVENT SHALL WILEY OR ITS LICENSORS BE LIABLE TO YOU OR ANY OTHER PARTY OR ANY OTHER PERSON OR ENTITY FOR ANY SPECIAL, CONSEQUENTIAL, INCIDENTAL, INDIRECT, EXEMPLARY OR PUNITIVE DAMAGES, HOWEVER CAUSED, ARISING OUT OF OR IN CONNECTION WITH THE DOWNLOADING, PROVISIONING, VIEWING OR USE OF THE MATERIALS REGARDLESS OF THE FORM OF ACTION, WHETHER FOR BREACH OF CONTRACT, BREACH OF WARRANTY, TORT,

NEGLIGENCE, INFRINGEMENT OR OTHERWISE (INCLUDING, WITHOUT LIMITATION, DAMAGES BASED ON LOSS OF PROFITS, DATA, FILES, USE, BUSINESS OPPORTUNITY OR CLAIMS OF THIRD PARTIES), AND WHETHER OR NOT THE PARTY HAS BEEN ADVISED OF THE POSSIBILITY OF SUCH DAMAGES. THIS LIMITATION SHALL APPLY NOTWITHSTANDING ANY FAILURE OF ESSENTIAL PURPOSE OF ANY LIMITED REMEDY PROVIDED HEREIN.

- Should any provision of this Agreement be held by a court of competent jurisdiction to be illegal, invalid, or unenforceable, that provision shall be deemed amended to achieve as nearly as possible the same economic effect as the original provision, and the legality, validity and enforceability of the remaining provisions of this Agreement shall not be affected or impaired thereby.
- The failure of either party to enforce any term or condition of this Agreement shall not constitute a waiver of either party's right to enforce each and every term and condition of this Agreement. No breach under this agreement shall be deemed waived or excused by either party unless such waiver or consent is in writing signed by the party granting such waiver or consent. The waiver by or consent of a party to a breach of any provision of this Agreement shall not operate or be construed as a waiver of or consent to any other or subsequent breach by such other party.
- This Agreement may not be assigned (including by operation of law or otherwise) by you without WILEY's prior written consent.
- Any fee required for this permission shall be non-refundable after thirty (30) days from receipt by the CCC.
- These terms and conditions together with CCC's Billing and Payment terms and conditions (which are incorporated herein) form the entire agreement between you and WILEY concerning this licensing transaction and (in the absence of fraud) supersedes all prior agreements and representations of the parties, oral or written. This Agreement may not be amended except in writing signed by both parties. This Agreement shall be binding upon and inure to the benefit of the parties' successors, legal representatives, and authorized assigns.
- In the event of any conflict between your obligations established by these terms and conditions and those established by CCC's Billing and Payment terms and conditions, these terms and conditions shall prevail.
- WILEY expressly reserves all rights not specifically granted in the combination of (i) the license details provided by you and accepted in the course of this licensing transaction, (ii) these terms and conditions and (iii) CCC's Billing and Payment terms and conditions.
- This Agreement will be void if the Type of Use, Format, Circulation, or Requestor Type was misrepresented during the licensing process.
- This Agreement shall be governed by and construed in accordance with the laws of the State of New York, USA, without regards to such state's conflict of law rules.

Any legal action, suit or proceeding arising out of or relating to these Terms and Conditions or the breach thereof shall be instituted in a court of competent jurisdiction in New York County in the State of New York in the United States of America and each party hereby consents and submits to the personal jurisdiction of such court, waives any objection to venue in such court and consents to service of process by registered or certified mail, return receipt requested, at the last known address of such party.

WILEY OPEN ACCESS TERMS AND CONDITIONS

Wiley Publishes Open Access Articles in fully Open Access Journals and in Subscription journals offering Online Open. Although most of the fully Open Access journals publish open access articles under the terms of the Creative Commons Attribution (CC BY) License only, the subscription journals and a few of the Open Access Journals offer a choice of Creative Commons Licenses. The license type is clearly identified on the article.

The Creative Commons Attribution License

The [Creative Commons Attribution License \(CC-BY\)](#) allows users to copy, distribute and transmit an article, adapt the article and make commercial use of the article. The CC-BY license permits commercial and non-

Creative Commons Attribution Non-Commercial License

The [Creative Commons Attribution Non-Commercial \(CC-BY-NC\) License](#) permits use, distribution and reproduction in any medium, provided the original work is properly cited and is not used for commercial purposes.(see below)

Creative Commons Attribution-Non-Commercial-NoDerivs License

The [Creative Commons Attribution Non-Commercial-NoDerivs License \(CC-BY-NC-ND\)](#) permits use, distribution and reproduction in any medium, provided the original work is properly cited, is not used for commercial purposes and no modifications or adaptations are made. (see below)

Use by commercial "for-profit" organizations

Use of Wiley Open Access articles for commercial, promotional, or marketing purposes requires further explicit permission from Wiley and will be subject to a fee.

Further details can be found on Wiley Online Library
<http://olabout.wiley.com/WileyCDA/Section/id-410895.html>

Other Terms and Conditions:

v1.10 Last updated September 2015

Questions? customercare@copyright.com.



Curriculum Vitae

Name: Yuki Bao

Post-secondary Education and Degrees: University of Western Ontario
 London, Ontario, Canada
 2018-2022 B.Sc. (Medical Biophysics, Medical Sciences)

The University of Western Ontario
 London, Ontario, Canada
 2022-2024 M.Eng. (Biomedical Engineering)

Honours and Awards: Continuing Admissions Scholarship
 The University of Western Ontario
 2018-2022

Dean's Honor List
 The University of Western Ontario
 2018-2022

Undergraduate Research Student Internships (USRI)
 2020-2022

Dean's Undergraduate Research Opportunity Program (DUROP)
2020

Related Work

Student Research Assistant

Experience

Poepping Lab for Biofluidics Research

The University of Western Ontario

2018-2024

Student Co-Author & Research Assistant

Frisbee-Goldman Lab Collaboration

The University of Western Ontario

2021-2022

Undergraduate Lab Assistant

Susan Vitali-Lovell Laboratory for Studies in Fetal Programming
of Human Health Risks

The University of Western Ontario

2018-2020

Undergraduate Research Assistant

Dr. Donald Saklofske's Lab in Personality and Measurement

The University of Western Ontario

2018-2019

Student Research Assistant

WLU Child Memory Lab at BRAINWORX

Wilfrid Laurier University

2017

Publications:

1. **Halvorson BD, Bao Y, Singh KK, Frisbee SJ, Hachinski V, Whitehead SN, Melling CWJ, Chantler PD, Goldman D, Frisbee JC.** Thromboxane-induced cerebral microvascular rarefaction predicts depressive symptom emergence in metabolic disease. *Journal of Applied Physiology* 136: 122–140, 2024. doi: [10.1152/jappphysiol.00410.2023](https://doi.org/10.1152/jappphysiol.00410.2023).
2. **Halvorson BD, Bao Y, Ward AD, Goldman D, Frisbee JC.** Regulation of Skeletal Muscle Resistance Arteriolar Tone: Integration of Multiple Mechanisms. *J Vasc Res* 60: 245–272, 2023. doi: [10.1159/000533316](https://doi.org/10.1159/000533316).
3. **Huang SJY, Wang X, Halvorson BD, Bao Y, Frisbee SJ, Frisbee JC, Goldman D.** Laser Doppler Fluximetry in Cutaneous Vasculature: Methods for Data Analyses. *J Vasc Res* : 1–15, 2024. doi: [10.1159/000538718](https://doi.org/10.1159/000538718).
4. **Schonberger ZG, Huang SJY, Thakkar RN, Mamone AA, Khan DI, Chow NLY, Ahmed M, Sivaram N, Bao Y, Kesavan V, Côté J, Sun C, Chhina J, Halvorson BD, Alimorad GH, Menon NJ, Goldman D, Frisbee SJ.** Assessments of Perfusion, Blood Flow, and Vascular Structure in Ambulatory Subjects: Guidance for Translational Research Scientists. *J Vasc Res* 60: 12–68, 2023. doi: [10.1159/000527765](https://doi.org/10.1159/000527765).
5. **Bao Y, Frisbee AC, Frisbee JC, Goldman D.** A constrained constructive optimization model of branching arteriolar networks in rat skeletal muscle. *Journal of Applied Physiology* 136: 1303–1321, 2024. doi: [10.1152/jappphysiol.00896.2023](https://doi.org/10.1152/jappphysiol.00896.2023).

Conferences and Seminars:

1. Bao Y. Microvascular Regulation between Two Hemodynamic Steady States in the Forearm and Forehead using Wavelet Phase Coherence. Poster presented at: Undergraduate Summer Research Internship (USRI); August 16, 2022; University of Western Ontario.

2. Bao Y. Constructing fractal networks to study microvascular physiology and pathophysiology in rat skeletal muscle. Presentation presented at: SCTPLS 2023 Annual Conference; August 3, 2023; University of Toronto.
3. Bao Y. Computational Generation of Arteriolar Networks Based on Constrained Constructive Optimization. Presentation presented at: 2024 CAP Congress; June 30, 2024; University of Western Ontario.